ERRATA SHEET

ESSA Technical Memorandum IERTM-NSSL-43

DETECTION AND PRESENTATION OF SEVERE THUNDERSTORMS
BY AIRBORNE AND GROUND-BASED RADARS:
A COMPARATIVE STUDY

K. E. Wilk, J. K. Carter, and J. T. Dooley

On page 6, Figure 1, captions should read:

a. Cold occlusion

b. Warm sector

c. Squall line

d. Stationary front

U.S. DEPARTMENT OF COMMERCE
ENVIRONMENTAL SCIENCE SERVICES ADMINISTRATION
RESEARCH LABORATORIES

ESSA Technical Memorandum ERLTM-NSSL 43

DETECTION AND PRESENTATION OF SEVERE THUNDERSTORMS BY AIRBORNE AND GROUND-BASED RADARS: A COMPARATIVE STUDY

K. E. Wilk
J. K. Carter
J. T. Dooley

NATIONAL SEVERE STORMS LABORATORY
NORMAN, OKLAHOMA
February 1969

TABLE OF CONTENTS

		Page
ABSTRACT		iv
1.	INTRODUCTION	1
2.	DATA COLLECTION	2
3.	THEORETICAL ATTENUATION CALCULATIONS	4
4.	ASPECT AND FLIGHT ALTITUDE EFFECT ON STORM INTENSITY MEASUREMENTS	10
5.	AN EFFECT OF ATTENUATION ON STORM TOP MEASUREMENT	12
6.	AIRBORNE MEASUREMENTS WITH X- AND C-BAND RADARS	14
7.	COMMENTS ON THE COMPARISON OF THE ARSR-1D AND WSR-57 DISPLAYS AND THE DETECTION OF LIGHTNING BY THE ARSR-1D	22
8.	CASE STUDY - 30 APRIL 1967	27
9.	CASE STUDY - 5 MAY 1967	43
10.	CONCLUSIONS	54
ACKNOWLEDGEMENTS		55
REFERENCES		55

ABSTRACT

Observations of severe thunderstorms by a WSR-57 radar are compared with PPI displays obtained simultaneously with Collins X- and C-band, and Bendix K_a-band airborne radars, and with the ARSR-1D air traffic control radar used by the FAA. Reflectivity estimates based on the S-band WSR-57 radar are used to evaluate the effects on core measurements by intervening precipitation.

Problems of beam aspect and flight altitude are discussed in relation to the storm reflectivity profiles encountered during the test flights. Comparative presentations are analyzed in detail for three of the storms investigated, and examples of contour mapping and lightning detection with the ARSR-1D radar are given.

The data indicate that precipitation attenuation of C- and X-band signals should not prevent their use for storm avoidance. Attenuation at the K_a-band is excessive, and use of this band is not advisable at middle and low flight altitudes. With the relatively narrow beam available at K_a-band, however, and an optional RHI presentation, this system offers a significant improvement in presentation and lessens the ambiguities caused by antenna tilt and beam aspect.

General agreement between displays of airborne and air traffic control radars should lead to similar conclusions by the pilot and controller concerning the location of hazardous weather. Since reflectivity measurements are highly sensitive to viewing aspect, however, it is extremely difficult to develop criteria applicable operationally for relating reflectivity measurements made with airborne radar systems to the measurements given by ground-based systems.

DETECTION AND PRESENTATION OF SEVERE THUNDERSTORMS BY AIRBORNE AND GROUND BASED RADARS: A COMPARATIVE STUDY

K. E. Wilk, J. K. Carter, and J. T. Dooley*

1. INTRODUCTION

The performance of airborne radar systems in detecting hazardous weather has been the subject of several studies. Marshall (1965) approached the problem of airborne radar detection and avoidance of severe weather theoretically, based on a statistical evaluation of observed severe storms and practical limitations of existing radars. His conclusions, drawn from consideration of model storms, wavelength, beam width, antenna size, and aircraft position relative to the storm, were: (a) a C-band system maintained at peak performance could adequately detect and resolve severe storm patterns without serious errors in intensity measurements arising from attenuation by precipitation; (b) an X-band system would be a first compromise, with increasingly dangerous attenuation effects overshadowing decreased beam size and increased sensitivity; (c) a K_a-band (35 gHz) radar would suffer intolerable attenuation effects and should not be considered as a primary storm avoidance system.

Merritt (1967) presented a model storm from which he estimated airborne radar weather detection performance theoretically. He compared these estimates with data obtained by the improved RDR-1E X-band airborne radar and the NSSL WSR-57 radar in air mass convective thunderstorms of moderate intensity with cell diameters of 4 to 8 n mi and tops of 35,000 to 40,000 ft. The data indicated that attenuation did not seriously limit the identification of the moderately intense thunderstorms investigated. Merritt's conclusions were that detection and storm reflectivity resolution capabilities of the airborne radars varied with aircraft altitude, as summarized in table 1. Results of the RDR-1E data collection program fell within the limits of the theoretical predictions.

Serving as a complement to Merritt's study, this report presents the results of data collected by L-, S-, C-, X-, and K_a-band radars. A statistical evaluation of attenuation effects in Oklahoma thunderstorms at selected wavelengths is included.

It is the purpose of this report to illustrate and describe comparative observations which are judged to be representative of the simultaneous displays of moderate and severe thunderstorms by airborne, control, and weather radars. The information summarized in this report contributes to general knowledge of the use of operational radars in observing thunderstorms.

---

*This work received substantial support from the FAA under Project Agreement No. FA65WAI-91.

Table 1. Effective range of airborne radar for detecting, identifying, and resolving moderate thunderstorms (after Merritt).

Altitude x(1,000 ft)	Range of Detection (N Mi)	Range of Pattern Identification (N Mi)	Range of Intensity Resolution (N Mi)
30-40	200-300	125-175	75
20-30	175-250	100-150	50-100
10-20	150-200	75-125	30-70

2. DATA COLLECTION

Data were collected from March through June 1967. The WSR-57 at NSSL, an FAA ARSR-1D at Oklahoma City, and airborne X-, C-, and K_a-band radars were used. The K_a-band, AMR-150A radar is 14 db more sensitive than the WSR-57, which was the radar used for reference. The ARSR-1D, WP-103, and WP-101 are 14 db, 17 db, and 19 db less sensitive than the WSR-57, respectively. Characteristics of these radars are detailed in table 2. The NSSL WSR-57 S-band radar, described by Clark and Dooley (1965) and Wilk et al. (1967), was accurately calibrated and its 10-cm wavelength is not subject to appreciable attenuation. Data were collected at zero-degree antenna tilt in normal operation, with 2° interval tilt sequences on the hour and at other selected times to obtain vertical reflectivity profiles of particular storms.

Airborne radar data were taken with the Collins WP-101 (C-band) and WP-103 (X-band) radars installed in a P-38 aircraft operated under contract with FAA. Calibration data supplied by Collins Radio Co. were the basis for our computations. Almost all the airborne data were taken at an altitude of 12,000 to 15,000 ft with zero-degree antenna tilt. Automatic attenuators were installed on the radars with the step attenuation averaging 5 db over a 25-db range. Airborne data were also supplied by a Bendix AMR-150A, K_a-band radar mounted in an Air Force RB-57C aircraft. There is no echo intensity data for this system, since it was not equipped with step attenuators. Although flights were often conducted in cloud, all flights remained outside significant precipitation. Therefore, none of the data in this report include possible effects of a water or ice film on the radome.

Data for the assessment of the weather detection capability of the FAA radar were taken with the ARSR-1D, instrumented as described by Wilk Dooley, and Kessler (1965), with the addition of an NSSL signal processor. Data used for the statistical evaluation of the attenuation effect of Oklahoma thunderstorms were taken with the WSR-57 radar digital syste described by Wilk et al. (1967).

Table 2. Characteristics of the radars employed in this study

Parameter	WSR-57 (Weather Radar)	WP-101 (Airborne)	WP-103 (Airborne)	AMR-150A (Airborne)	ARSR-1D (Control Radar)
Wavelength (cm)	10	5.5	3.2	0.86	23
Power P_t (kW)	400	75	20	120	400[1]
Ant. gain G (db)	38.3	27.5	30	47	34.3
Pulse length h(μs)	4	2.1	2.3	1	2
MDS (dbm)	-108	-104	-105	-103	-109
PRF (pps)	164	400	400	400	360
Range (n mi)	250	150	150	100	200
θ_h (deg)	2	7.5	4.9	0.75	1.4
θ_v (deg)	2	7.5	4.9	0.75	6.2
Polarization	linear	linear	linear	linear	linear or circular
Minimum Detectable Z_e at 100 n mi, mm^6m^{-3}	3.5	290	193	0.15[2]	91
Radar const.[3] (Wilk-Dooley)	$1.13(10^{-16})$	$1.83(10^{-17})$	$8.2(10^{-17})$	$2.76(10^{-14})$	$3.48(10^{-8})$
(Merritt)[4]	$4.88(10^{-11})$	$1.54(10^{-12})$	$1.79(10^{-12})$	$3.81(10^{-9})$	$1.06(10^{-12})$

[1]A factor of 10 greater with amplitron.

[2]Neglecting atmospheric attenuation.

[3]The radar const. $C = 1.78 \times 10^{-28} G^2 \theta_h \theta_v h \pi^5 |K|^2 \lambda^{-2}$, is an overall measure of performance of the radar system.

[4]Merritt retained $|K|^2$ as a variable and included P_t in the radar constant.

Table 3. Dates flown and types of airborne radar data acquired

Date	Radar	Date	Radar
18 Apr	K_a	12 May	X
25 Apr	K_a	13 May	X
29 Apr	K_a	27 May	X and C
30 Apr	K_a	28 May	X and C
3 May	K_a	30 May	X and C
5 May	K_a, X, and C	19 Jun	X and C
6 May	K_a, X, and C	21 Jun	X and C

Table 3 lists the dates of the flights on 14 days between 18 April and 21 June and the type of radar data collected.

The P-38 aircraft (X- and C-band radars) was based near Dallas, Texas, which is approximately 40-min flying time from NSSL. The B-57 aircraft (K_a-band radar) was based near Albuquerque, New Mexico. Although several different flight profiles had been planned, it proved more expedient to route both aircraft directly to NSSL and, upon arrival select simple, straight-line approaches to the precipitation system existing at that time. During data collection, the aircraft were in radio communication with an FAA controller stationed at NSSL and were flight controlled and tracked with a modified CPN-18 air traffic control radar.

The most informative flights occurred on 30 April and 19 June. High-quality data also were collected on 5 May and 21 June. Two flights were examined in detail and are discussed in the sections that follow.

3. THEORETICAL ATTENUATION CALCULATIONS

Theoretical attenuation values in db km^{-1} were computed as a function of rainfall rate and radar wavelength. The digitized WSR-57 radar data in B-scan format (Wilk et al., 1967) served as input in these computer calculations. The relationships found by Ryde (1946), Gunn and East (1954), and Hitschfeld and Bordan (1954), and summarized by Battan (1959) were used to determine the two-way attenuation corresponding to various values of log Z_e*. Table 4 lists the log Z_e, equivalent rainfall rate, and corresponding attenuation values for the three wavelengths studied.

*The radar reflectivity factor Z_e, discussed in the references, measures the summation of precipitation particle diameters to the sixth power, per unit volume, and increases with storm severity, as shown in table 4

The WSR-57 digital records collected during the spring of 1967 were scanned subjectively for echo distributions that would be statistically representative of severe weather patterns in Oklahoma. A B-scan digital recording of the 5 May storm (fig. 1d) is shown in figure 52, section 9. Each horizontal line in the digital data encompasses a range from 20 to 100 n mi along a particular azimuth. Each integer represents the logarithm of the reflectivity factor Z_e in range increments of 1.4 n mi.

The computer summary, illustrated in figure 2, was obtained from the intensity integers for each 2° azimuth as follows:

1. The line of integers was scanned to find the maximum integer present at any range. This value was then defined as the storm core. If the maximum was represented by two or more equal integers, the first maximum after the start of a line was treated as a core in subsequent analysis for starts at both ends of the line.

2. Starting at a range of 20 n mi, all integers existing out to the first core value encountered were translated to attenuation values and summed. The total attenuation (summed from the left) and the incremental attenuation were listed. The running total was subtracted from the core value and listed for each integer, or range step.

3. The calculations were repeated, but with decreasing range (summed from the right), starting at 130 n mi and approaching the first core value encountered from the far end of the line.

Table 4. Attenuation and rainfall rate values corresponding to the six levels of echo reflectivity monitored

Log Z	Approximate Rainfall Rate (mm hr^{-1})	Attenuation, db km^{-1} (one way)		
		K_a	X	C
1	0.15	0.03	0.0006	.0002
2	0.65	0.14	0.004	.0013
3	2.7	0.60	0.027	.0071
4	11.5	2.54	0.182	.0384
5	48.6	10.70	1.199	.2070
6	205	45.11	7.902	1.1150

COLD OCCLUSION

a. ~~Squall line~~ - 11 April 1967

WARM SECTOR

b. ~~Stationary front~~ - 5 May 1967

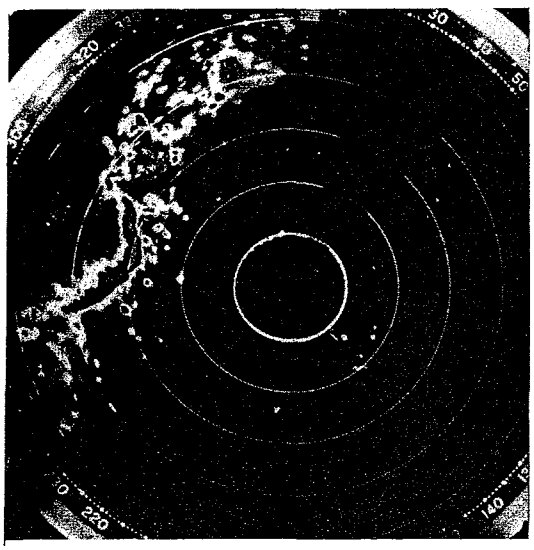

SQUALL LINE

c. ~~Warm sector~~ - 20 April 1967

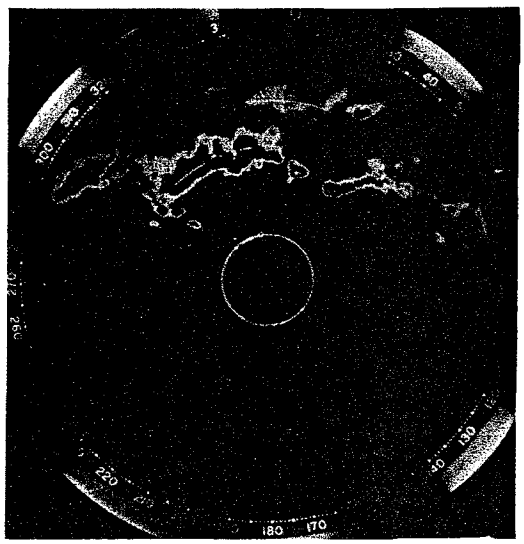

STATIONARY FRONT

d. ~~Cold occlusion~~ - 25 April 1967

Figure 1. Samples of WSR-57 radar data used in the attenuation computations. Synoptic type refers to depiction by ESSA Weather Bureau operational charts.

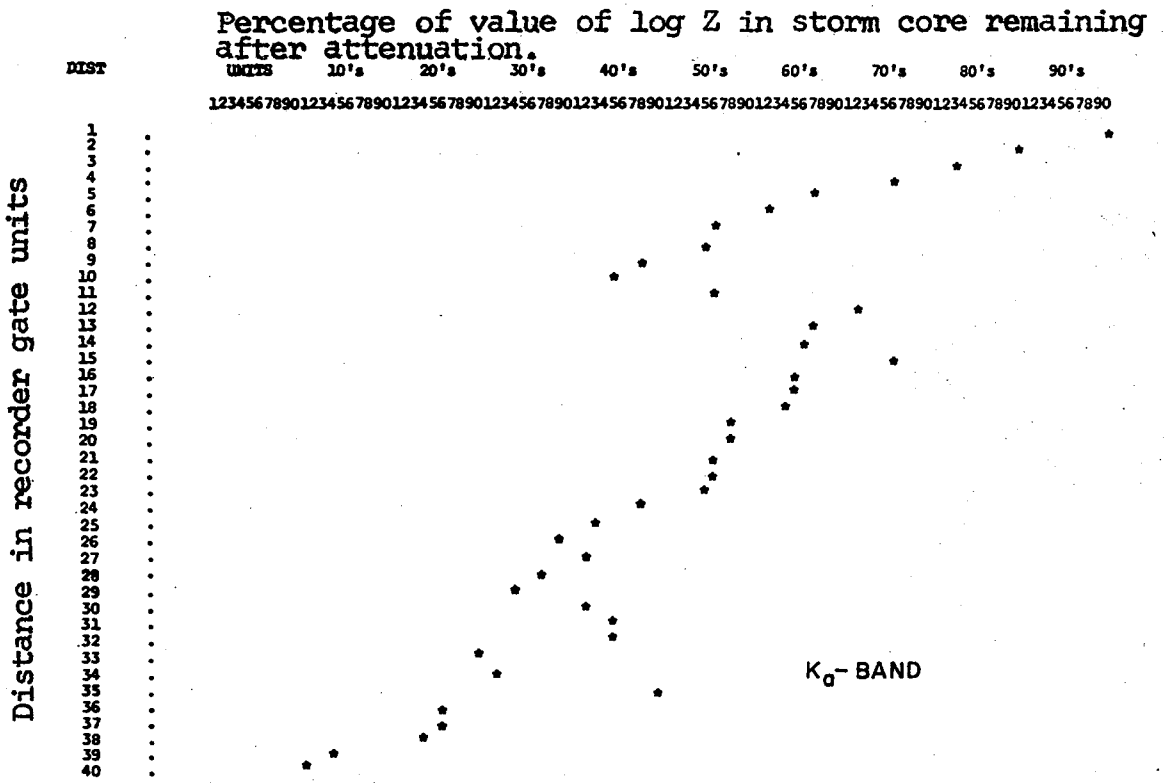

Figure 2. Computer listing of the calculation of the effect of attenuation computations for K_a-band radar. With $Z_e = 200\ R^{1.6}$ and attenuation, α, per unit distance as K_2R^r (Gunn and East, op. cit), the average percent remaining in the storm core value after attenuation is shown as a function of distance from the core. The distance column on the extreme left is expressed in recorder gate units, where one gate is 1.4 n mi.

4. All the azimuth calculations were combined to produce the frequency distribution of core value degradation as a function of distance from the storm core.

Approximately 2,000 azimuth listings were processed in this manner. Figure 3 shows the distribution of the log Z_e integers used. The mean Z_e value is $10^2 mm^6 m^{-3}$ with 8 percent of the values greater than $10^4 mm^6 m^{-3}$. The latter value is indicative of severe weather for most aircraft.

The effects of attenuation on the measurement of the storm cores for the C-, X-, and K_a-band radars are summarized in the graphs in figures 4, 5, and 6. At C-band (fig. 4), the core value (log Z_e) is decreased on the average by less than 1 percent out to a range of 10 units (14 n mi). That is, a core value of log Z_e = 5 is reduced to log Z_e = 4.95, and a core value of log Z_e = 4 is reduced to log Z_e = 3.96. At X-band (fig. 5), the same range of 14 n mi produces an attenuation of 2.2 percent and reduces log Z_e = 5 core to log Z_e = 4.9.

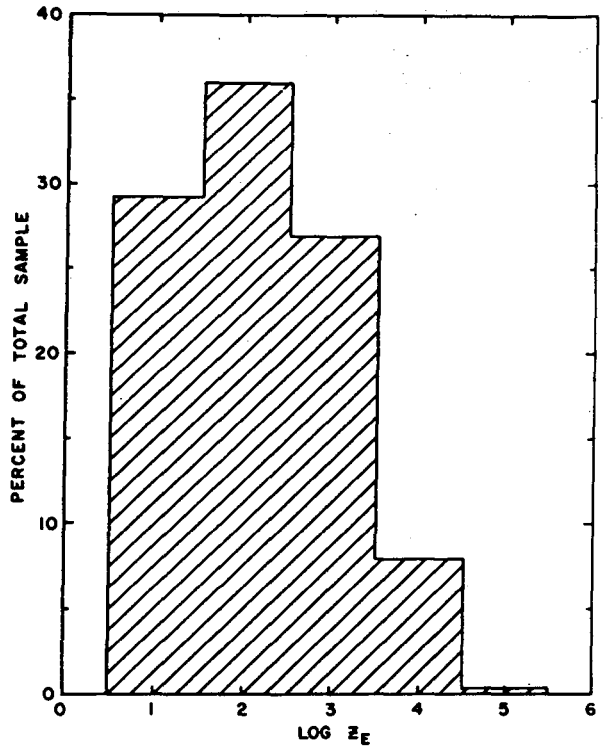

Figure 3. Frequency distribution of log Z_e values used in the calculation of attenuation.

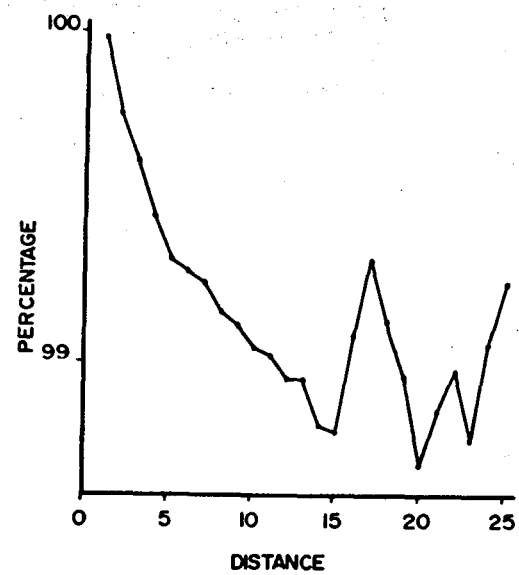

Figure 4. Average percentage decrease in storm core value of log Z_e for C-band radars as a function of distance from the storm core. (One unit of distance equals 1.4 n mi.) At a distance of 20 to 25 units (28 to 35 n mi), a core value of log Z_e = 4 (moderate rainfall), is reduced to log Z_e = 3.96.

The attenuation reaches 3 percent at approximately 25 range units (35 n mi). The K_a-band results (fig. 6) show the much greater effect corresponding to the large K_a-band coefficients listed in table 4. At a range of 14 n mi from the storm core, the logarithm of core value is decreased by 50 percent. This means that a log Z_e = 5 (severe storm) core is seen as log Z_e = 2.5 (light to moderate rain), and a log Z_e = 4 is reduced to log Z_e = 2. Obviously, both are unacceptable reductions for quantitative measurements. The maximum reduction at 42 n mi is 60 percent, which reduces log Z_e = 5 to log Z_e = 2.

The confidence level of these values is dependent not only on the representativeness of the log Z_e integers used, but also on the theoretical assumptions inherent in the attenuation calculations. Medhurst (1965) attempted experimental verification of Ryde's formula for K_a-band, and found greater attenuation than predicted. On the other hand, Mueller et al. (1967) calculated attenuation at the X-band from drop size data collected at Miami, Florida, and found less attenuation than predicted by Robertson and King (1946). Since the K_a-band attenuation shown in this study is already severe, no attempt was made to include Medhurst's findings. We recalculated the X-band attenuation using the linear regression found by Mueller in which values below

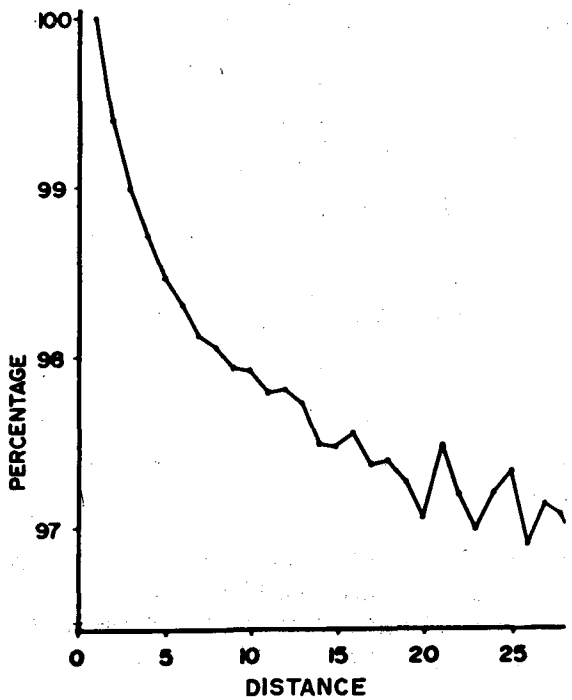

Figure 5. Average percentage decrease in storm core value of log Z_e for X-band radars as a function of distance from the storm core. (One unit of distance equals 1.4 n mi.) At a distance of 20 to 25 units (28 to 35 n mi), a core value of log Z_e = 4 (moderate rainfall), is reduced to log Z_e = 3.88.

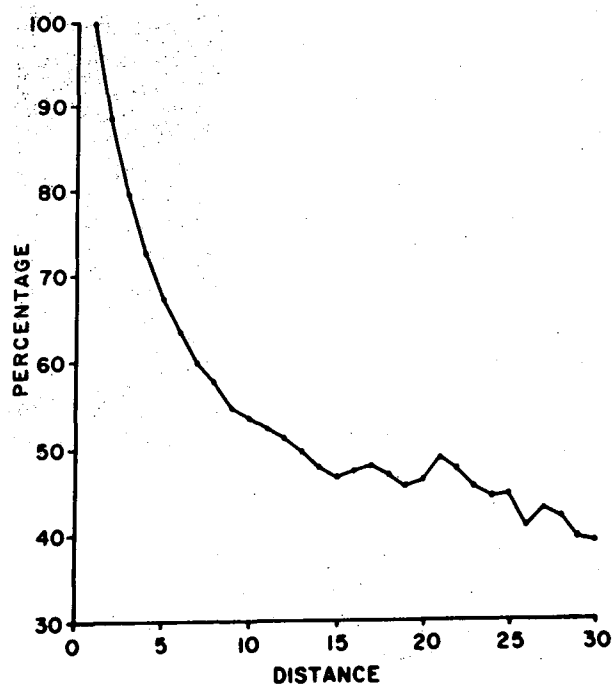

Figure 6. Average percentage decrease in storm core value of log Z_e for K_a-band radars as a function of distance from the storm core. (One unit of distance equals 1.4 n mi.) At a distance of 20 to 25 units (28 to 35 n mi), a core value of log Z_e = 4 (moderate rainfall), is reduced to log Z_e = 1.8.

$Z_e = 10^3 mm^6 m^{-3}$ were ignored. The results indicated only small changes in the effective range of storm core measurement.

It is emphasized that the analysis technique determines the average expected attenuation. Extreme values exist at a frequency directly related to the occurrences of $Z \geq 10^5 mm^6 m^{-3}$. Analysis of the NSSL hourly data for 1966 show this level occurs over 1/1000 of the area covered by $Z \geq 10 mm^6 m^{-3}$ in Oklahoma. This is a conservative estimate, owing to factors which degrade illumination of the precipitation target by the radar beam. Attenuation values corresponding to $Z \geq 10^5 mm^6 m^{-3}$ for a sample of the X-band data summarized in figure 5 were tabulated to estimate the maximum values expected. For 58 lines with $Z \geq 10^{5.0} mm^6 m^{-3}$, 46 were attenuated to $10^{4.5} mm^6 m^{-3}$, 11 were attenuated to $10^{4.0} mm^6 m^{-3}$, and one was attenuated to $10^{3.5} mm^6 m^{-3}$. These results are similar to conclusions by Marshall et al. (1965), which state that wavelength 3.2 cm lacks discrimination about storm intensity and size beyond a rainfall rate of 100 mm hr^{-1} ($Z = 10^{5.5} mm^6 m^{-3}$) and that, treating areas as single storms, 3.2 cm radar can be used for storm avoidance.

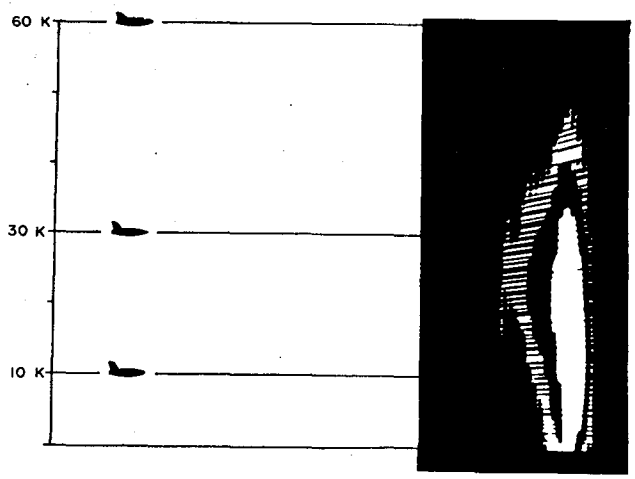

Figure 7a. Assumed flight profiles used in determining aspect biasing of reflectivity measurements.

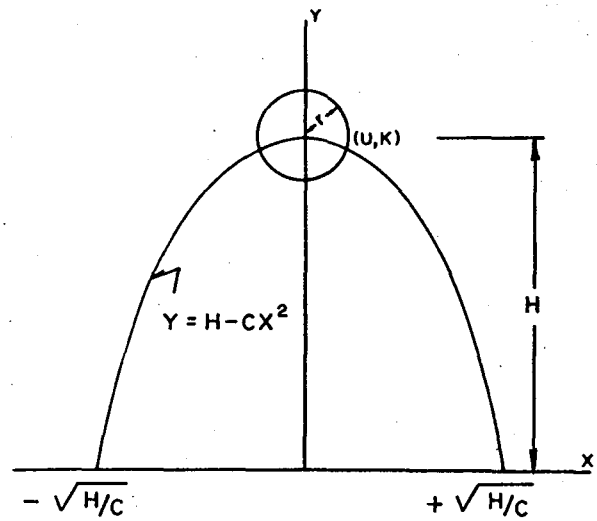

Figure 7b. Mathematical model used in aspect calculations. The real distribution was not symmetrical about the vertical axis.

4. ASPECT AND FLIGHT ALTITUDE EFFECT ON STORM INTENSITY MEASUREMENTS

Merritt (1967) has treated the beam-filling problem in detail and has shown the great complexity of interpreting airborne radar reflectivity measurements.

Applications of a simple radar and thunderstorm model to the case of a severe thunderstorm observed on 30 April illustrate the aspect problem inherent in aircraft observations. The three observed reflectivity profiles of $Z_e = 10$, 10^3, and $10^5 mm^6 m^{-3}$ were used as the weather target for simulated aircraft approaches. The aircraft was placed at 60,000, 30,000 and 10,000 ft respectively, with the range changed in each case from 100 n mi to 10 n mi. The radar antenna was assumed to be set to a constant downtilt angle so that the beam axis grazed the earth at 100 n mi. The antenna diameter was held constant at 22 in. so that the beam width increased with wavelength. Figure 7a illustrates the three assumed approaches at different altitudes toward the thunderstorm profile. A numerical approximation of these approaches was evaluated by assuming a quadratic best fit to the normalized* reflectivity profile, and by superimposing a circular airborne radar beam pattern, as shown in figure 7b.

If we assume that the aircraft is directed at the storm axis, the beam pattern cross section is

$$Y - (r^2 - x^2)^{\frac{1}{2}} - H ,$$

*The cross sectional area of the echo at various altitudes were used to define equivalent storm radii, which were then used in computing a parabolic best fit.

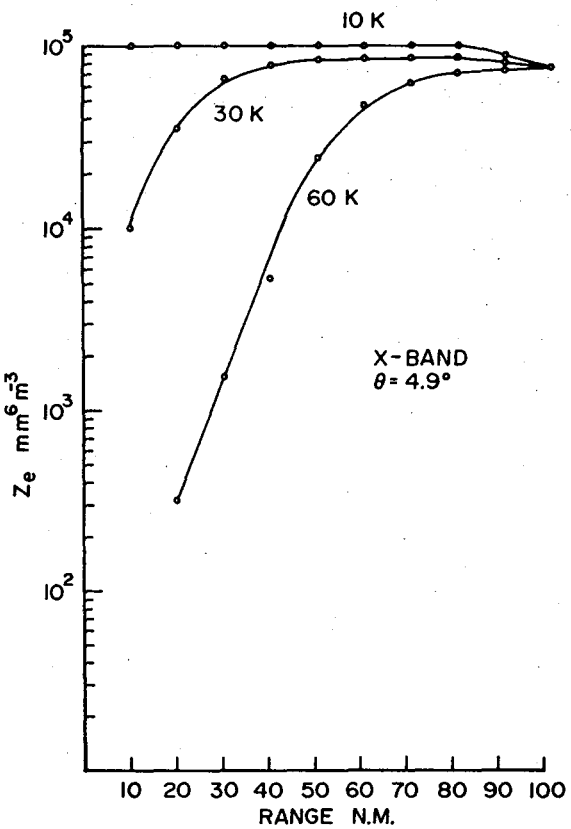

Figure 8. Expected X-band airborne radar reflectivity profiles during approach.

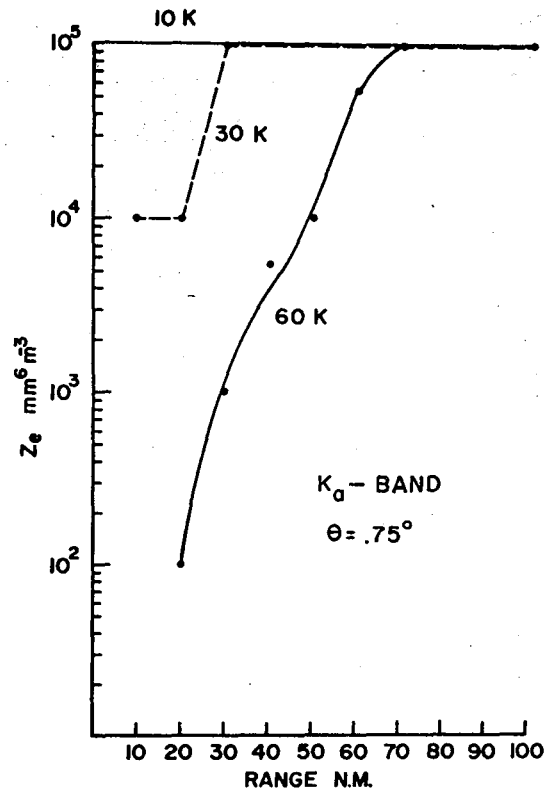

Figure 9. Expected K_a-band airborne radar reflectivity profiles during approach.

where H is the aircraft altitude. The common area, A, between the radar beam and a storm contour is

$$A = 2 \int_0^u \int_{(r^2-x^2)^{\frac{1}{2}} - H}^{H-cx^2} dydx \quad . \tag{1}$$

This equation was solved graphically for the degree of beam filling by each of the three Z_e contours. The apparent Z_e was found by summing the individual products of intercepted beam area and Z_e contour:

$$Z_A = \frac{A_1 Z_1}{A_t} + \frac{A_2 Z_2}{A_t} + \frac{A_3 Z_3}{A_t} \ , \tag{2}$$

where A_t is the total beam area.

Figure 8 shows a plot of the expected X-band radar reflectivity measurements as a function of range for the three altitudes. A slight beam-filling effect is noted at ranges from 100 to 80 n mi; for the remainder of the approach, varying aspect is the most serious source

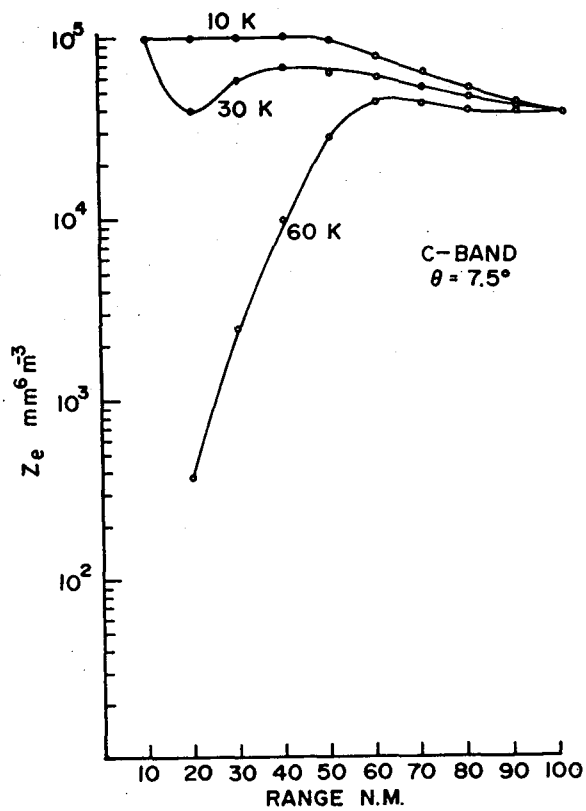

Figure 10. Expected C-band airborne radar reflectivity profiles during approach.

of bias. The beam overshoot is severe at a flight altitude of 60,000 ft, causing a 20-db decrease in apparent reflectivity at a range of 20 n mi. At 30,000 ft, the reflectivity remains within 10 db of the core value to a range of 10 n mi. At 10,000 ft, a representative storm core reflectivity is measured throughout the approach time from 80 n mi.

Because of the narrower beam, the aspect effect at the K_a-band is even more severe than at the X-band, as shown in figure 9. The change in apparent Z_e from 70 n mi to 20 n mi is 30 db. Beam filling is not a factor until well over 100 n mi. The sudden changes in reflectivity at 20 and 30 n mi arise from the stepped contours assumed for the model.

As shown in figure 10, the C-band radar has a more serious beam-filling problem. At 100 n mi, there is approximately a 5-db lowering of the apparent Z_e. At 60,000 ft, overshooting begins at 50 n mi and causes a reduction of 20 db at about 20 n mi. The sharp increase in reflectivity during the final 20 n mi is a peculiarity of the aircraft altitude and the assumed reflectivity contours. As in the case of the K_a-band, these sharp changes are not realistic, and are due only to the step function assumed for the model storm. The overshooting problem can, of course, be largely compensated for by increasing the antenna down tilt. However, positioning and signal interpretation require prior knowledge of the reflectivity profile of the storm. It may be possible to examine historical reflectivity data, including the statistical properties of radar echo distributions, and to select flight profiles on a statistical basis to optimize the accuracy in reflectivity data. As Merritt (1967) has stated, however, the problem is very complex and requires research beyond the scope of this project.

5. AN ATTENUATION EFFECT ON STORM TOP MEASUREMENT

When the aircraft is approaching a storm and the radar is operated in a RHI mode, the echo top measurement is affected by the intervening precipitation attenuation along the slant range to the top. This biasing is well illustrated by the severe thunderstorm on 30 April (see sec. 8).

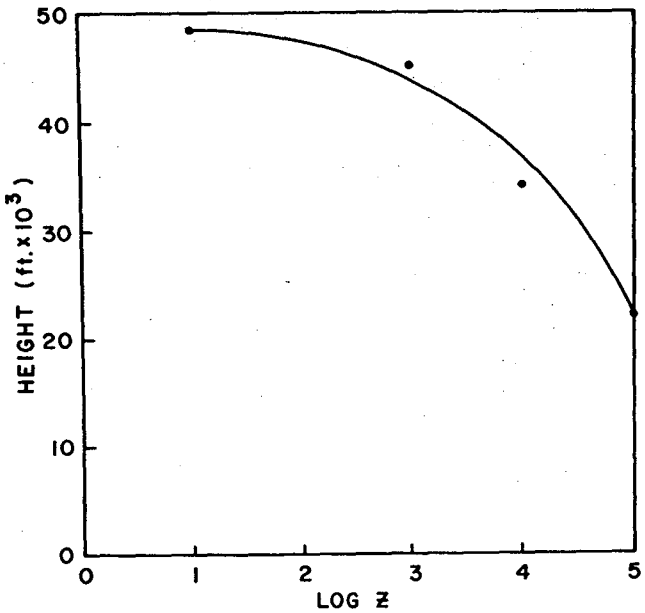

Figure 11. Reflectivity-height profile for the severe thunderstorm of 30 April 1967.

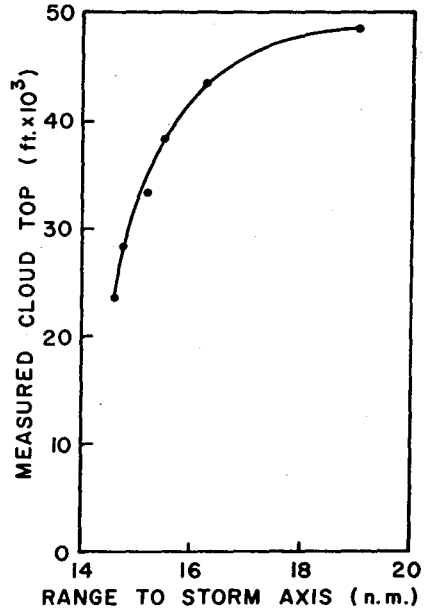

Figure 12. Apparent cloud top height as a function of range after theoretical attenuation is applied, for aircraft flying at 10,000 ft.

Ground radar measurements placed the storm top on 30 April 1967 at 48,500 ft. As in the preceding section, the WSR-57 contours were used to construct the vertical cross sections of the three radar reflectivity levels, $Z_e = 10$, 10^3, and $10^5 mm^6 m^{-3}$. The slant range cross sections of integrated signal attenuation were then computed for the airborne K_a-band radar at ranges of 5, 10, 15, and 20 n mi from the storm core. The averaged reflectivity profile used in these calculations is shown in figure 11. Table 5 lists the range, the two-way signal attenuation α, the K_a-band radar detection threshold, and the net excess or loss of signal as a function of range, for a plane flying at 10,000 ft.

For example, at a range of 20 n mi, the radar is capable of seeing a signal 34 db above a Z of $10 mm^6 m^{-3}$. However, the integrated attenuation of 28.4 db lowers this value to 5.6 db above the threshold of $10 mm^6 m^{-3}$. As the central storm top becomes shadowed by the lower level precipitation, the attenuation increases, and the detectable top is lowered correspondingly, as shown graphically in figure 12.

At 15 n mi from the storm core, the detectable echo top is reduced from 48,500 to 33,500 ft. Although not exact, these values caution against interpreting RHI measurements of thunderstorms at or near terminals and using these measurements for selection of climb-out routes.

Table 5. Effect of attenuation on K_a-band signal from cloud top as a function of range from storm core. Cloud top is 48,500 ft with $Z_e = 10 mm^6 m^{-3}$. Aircraft is flying at 10,000 ft

(1)	(2)	(3)	(3-2)
Aircraft range to storm core (n mi)	Two-way attenuation db	db above min detectable for unattenuated signal from cloud top	Calculated signal-to-noise ratio (db)
20	28.4	34	+5.6
15	71.2	37	-34.2
10	121.0	40	-81.0
5	138.6	44	-94.6

6. AIRBORNE MEASUREMENTS WITH X- AND C-BAND RADARS

A P-38 aircraft, provided under FAA contract by Mr. James Cook, Dallas, Texas, was equipped with Collins radars, types WP-101 and WP-103 (see fig. 13). The characteristics of these sets are listed in table 2. Mr. Cook used a 16-mm camera mounted to view two PPI displays. The scopes used standard daylight viewing cathode ray tubes frontlighted by photolamps and step IF attenuators* were cycled automatically to provide intensity profiles. STC circuits set to a normalization range of 30 n mi were used on both radars.

The simultaneous operation of the air traffic control and airborne and ground weather radars produced an interesting perspective of the differences and similarities in displays of the same thunderstorm complex. The airborne displays were normally operated on 60-n mi range and displayed a 60° sector ahead of the aircraft. This area was only 6 percent of that under surveillance by the ARSR-1D and WSR-57 radars, which operated on 360° scan with contour-mapped video displayed to a range of 100 n mi.

*Note the dual use of the word "attenuation." As discussed in section 3, radar energy can be absorbed by precipitation with a loss of signal incident on and scattered back from precipitation at greater ranges. In this section, we refer to a stepwise reduction of signal during successive PPI radar scans. By comparing photographs one can evaluate the echo intensity over the entire scanned region. This technique is widely used when contouring circuits are not available.

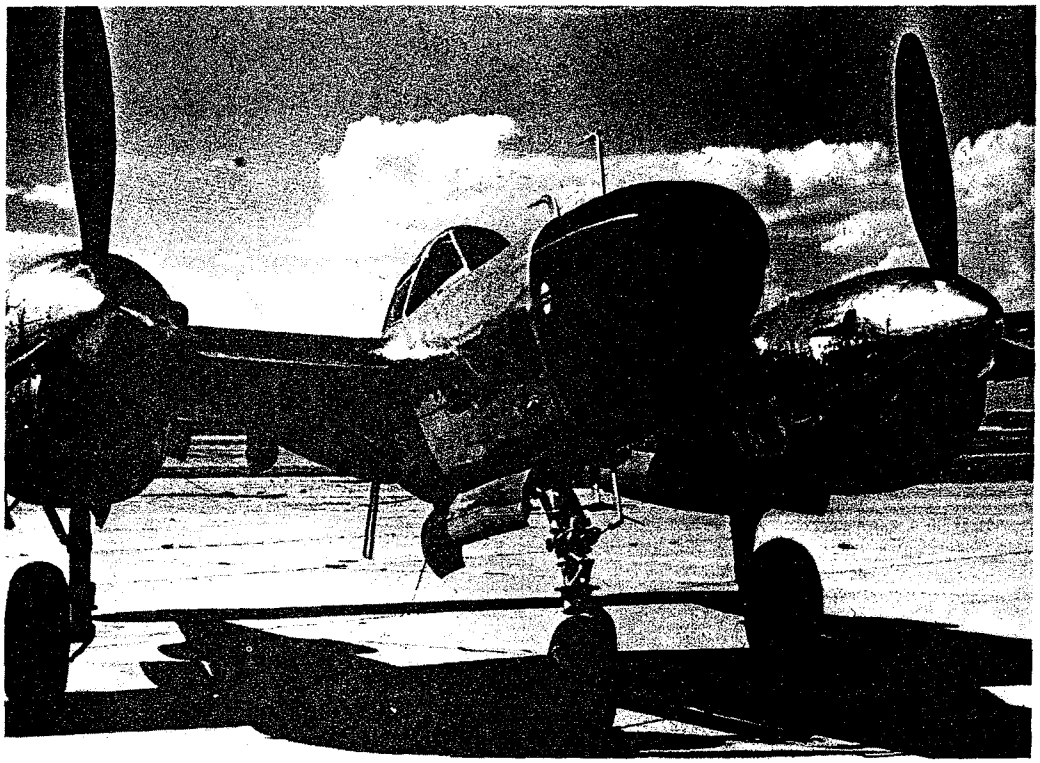

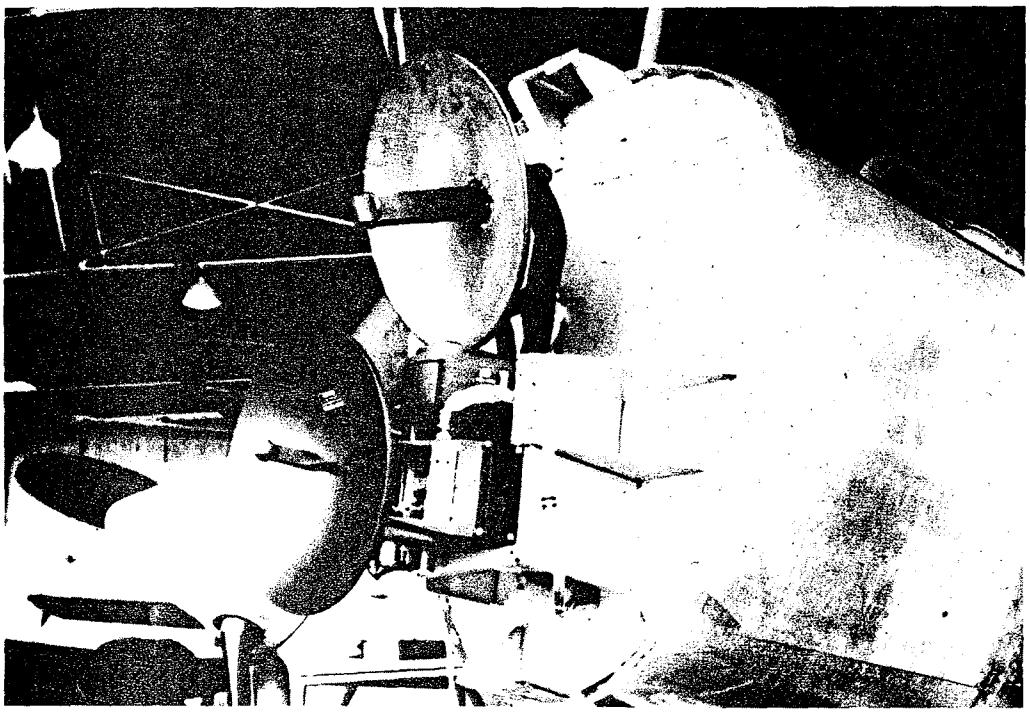

Figure 13. P-38 aircraft and twin airborne radar installation.

An example of the airborne radar displays is shown in figure 14a. The photograph of the full 16-mm frame contains both scopes, a compass and a clock. The left scope is the X-band radar display, and the right scope is the C-band radar display. The value of IF attenuation is displayed on a nixie light to the left of the clock. The airborne radars were looking northeast and displaying the western end of a line. The two series of photographs in figure 14b show photographs at 6-db steps of IF attenuation.

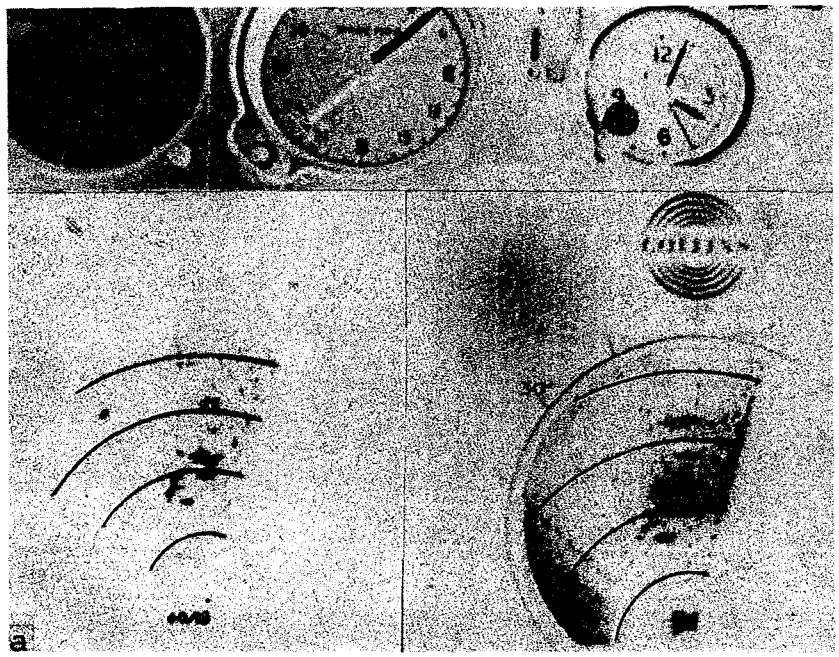

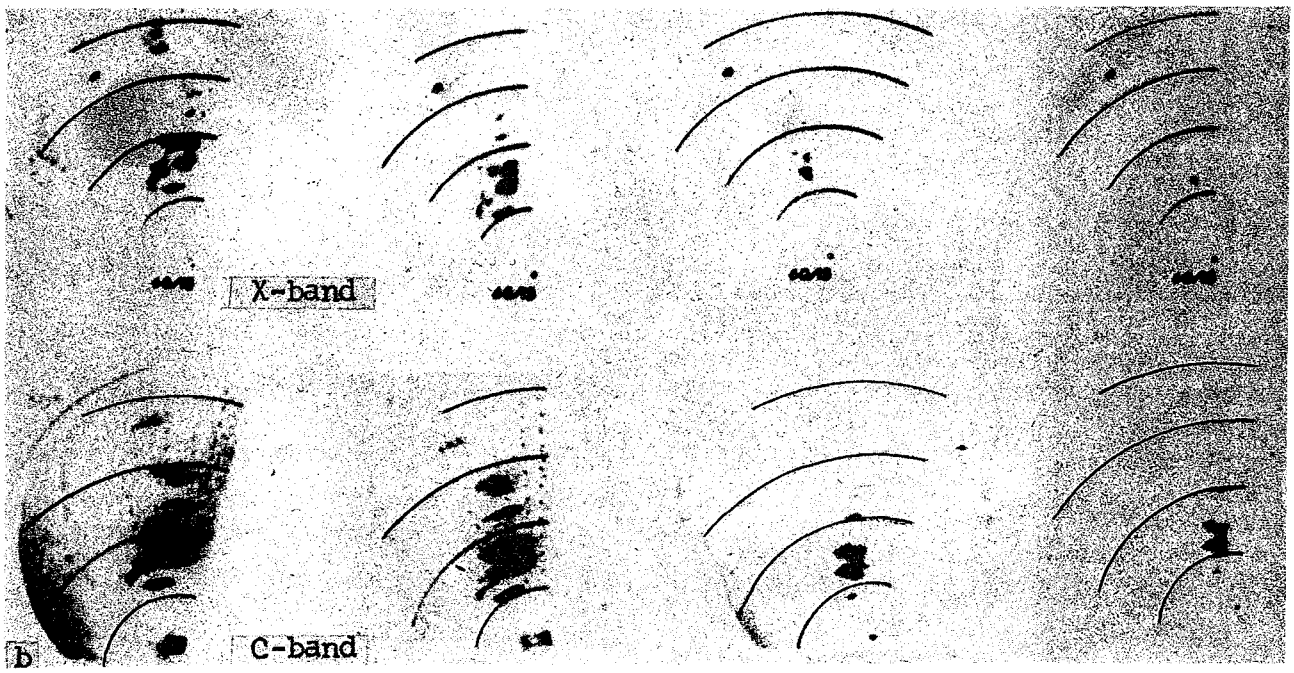

Figure 14. Airborne radar displays, 21 June 1967. Range marks are 15 n mi. Attenuation steps are approximately 6db 1504 CST

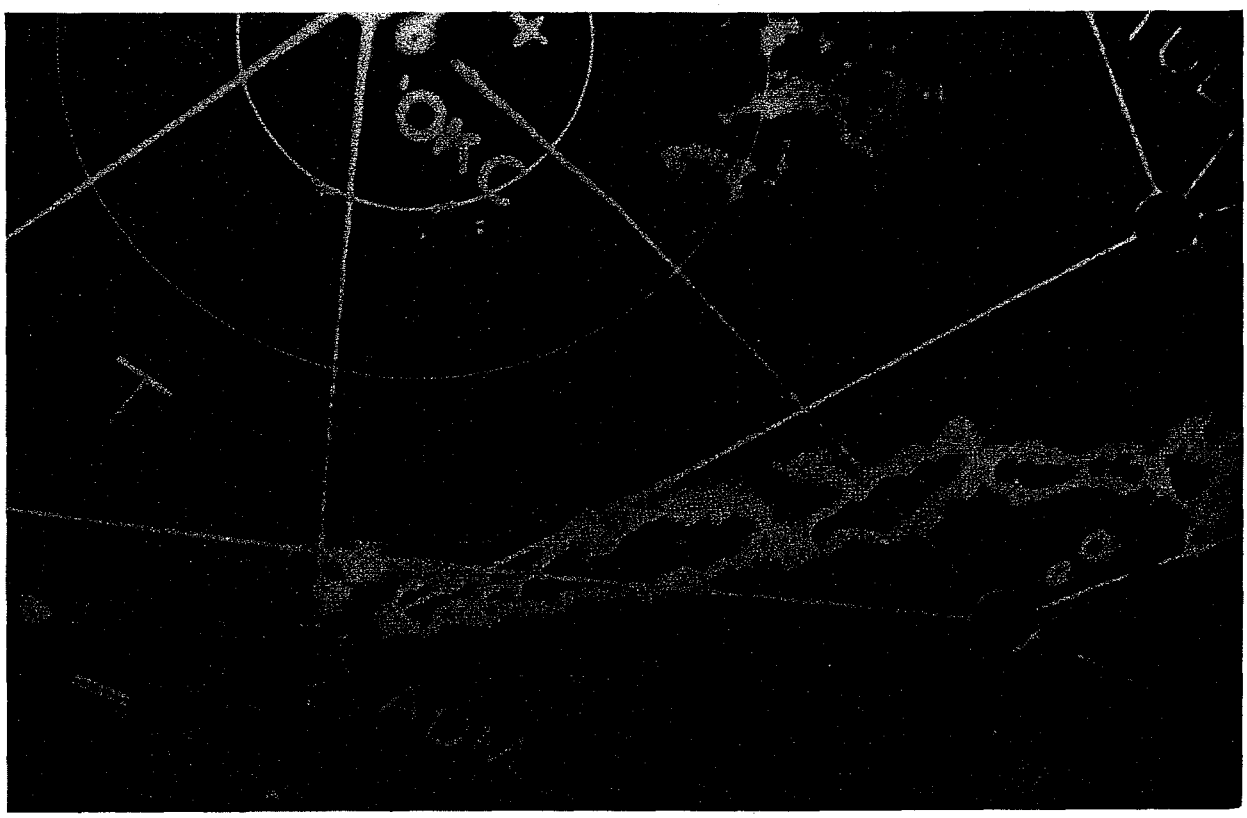

Figure 15. Control radar display, 21 June 1967.

The scope photograph in figure 15 shows the ARSR-1D air traffic control radar PPI at the FAA Academy at Will Rogers World Airport, 12 n mi northwest of NSSL on 21 June 1967. The IFF signal 20 n mi west of Ardmore (ADM) is from the P-38 as it began a data run. The track and time references are shown in figure 16. The three strip tilt sequence was obtained at 0, 2, and 4° with the NSSL WSR-57 weather radar. The altitudes of the beam axis for the tilt angles at the mean echo range (60 n mi) are 2,500, 15,000, and 28,000 ft, respectively.

Although the ARSR-1D and the WSR-57 radars are located 12 n mi apart, the agreement between the displays, as shown in figures 15 and 16, is excellent. Much of the echo configuration is well correlated, which makes it relatively simple to cross-reference the displays cell by cell. The contours are not matched in gray scale. The video cancellation on the WSR-57 is well matched with the video of intensity level 2 displayed by the ARSR-1D. The next intensity contour (light gray on the WSR-57 and cancellation on the ARSR-1D) represents a 10-db change in both radar displays. Again, the match is good. The final contour (bright return on the WSR-57 and light gray on the ARSR-1D) is not well matched. This difference (about 5 db) is caused primarily by drift in calibration of the signal processor quantizers. A slight shift in the log receiver response produces a corresponding shift in the displayed

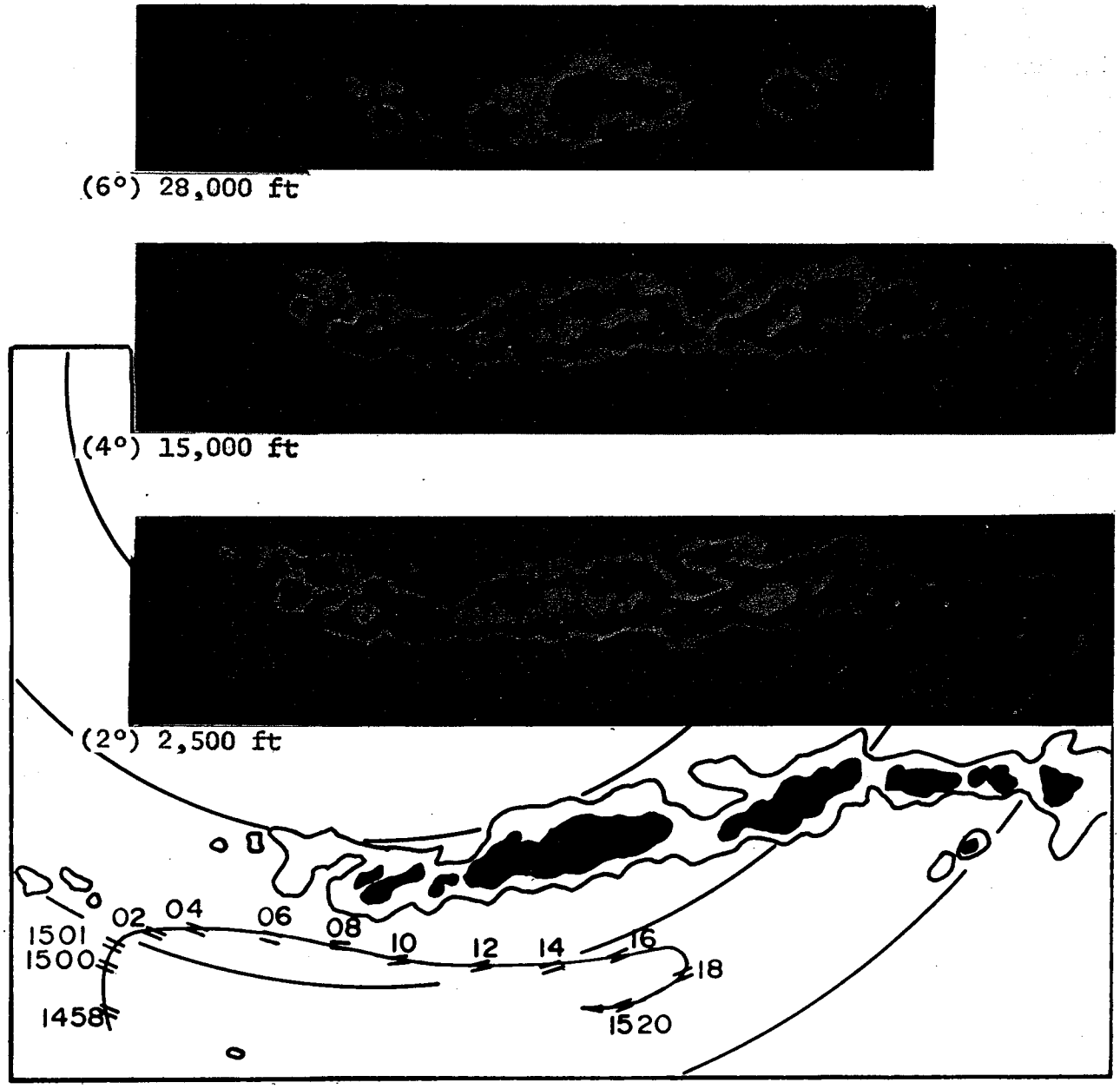

Figure 16. P-38 track and WSR-57 weather radar display, 21 June 1967.

levels, which is especially noticeable for very low or very high input signals. There is a small discrepancy (about 3 db on the average) caused by the differential beam filling between the two radars (Wilk et al., 1965). In this example, with the WSR-57 radar showing storm core reflectivities of $10^4 mm^6 m^{-3}$ to 28,000 ft, the ARSR-1D radar beam must be nearly filled. Therefore, the difference in this case is assumed to be the result of instrumentation.

It is very difficult to match the airborne displays in detail to the control and weather radars on the ground. The lack of contour mapping on the airborne displays is one hindrance in diagnosis, but the difference in perspective is of much greater consequence. Both the X- and C-band airborne radars depict a group of cells that are confined to the western end of the line. The extent of the line is not evident, and detailed cell-to-cell correlation with the ground radars is poor. The attenuated displays show the relative strengths of the clustered cells, and the location of the strongest cell agrees well with that displayed by the ground radars. That is, even though pattern recognition is lacking, the airborne and ground-based radars isolate the same location as being the most severe.

On 19 June, an isolated severe thunderstorm developed near Enid, Oklahoma. The P-38, which had been alerted at noon, flew over NSSL at 1650 CST and proceeded north toward the storm. The detailed track is shown in figure 17. Step attenuation sequences were started on both radars at 1700 CST 75 n mi from the storm and continued to a range of 20 n mi. Figure 18 shows the PPI display of the FAA ARSR-1D air traffic control radar, with NSSL signal integrator attached to provide contours. The transponder signal from the P-38 is visible 50 n mi south of the storm echo. The corresponding NSSL WSR-57 integrated displays acquired through an antenna tilt sequence are shown in figure 19. The bright core corresponds to a reflectivity of $6.3 \times 10^4 mm^6 m^{-3}$, or 8 db greater

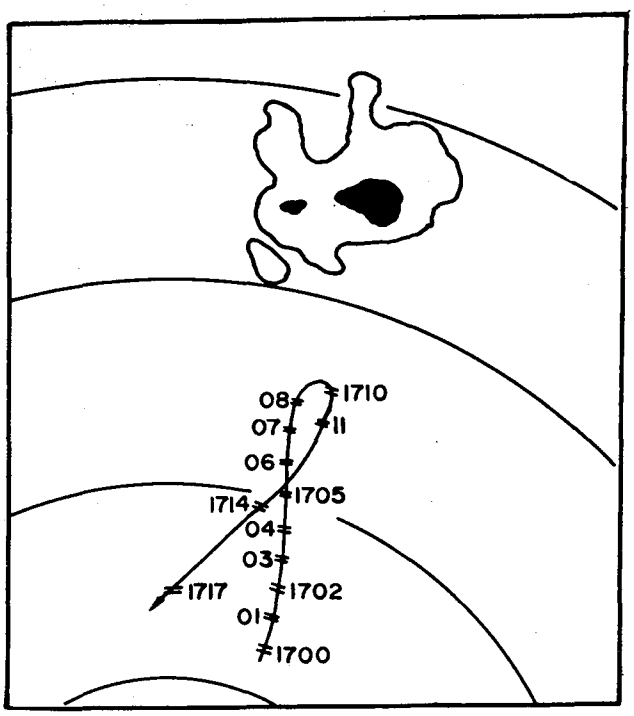

Figure 17. P-38 track, 19 June 1967. Range marks are 25 n mi.

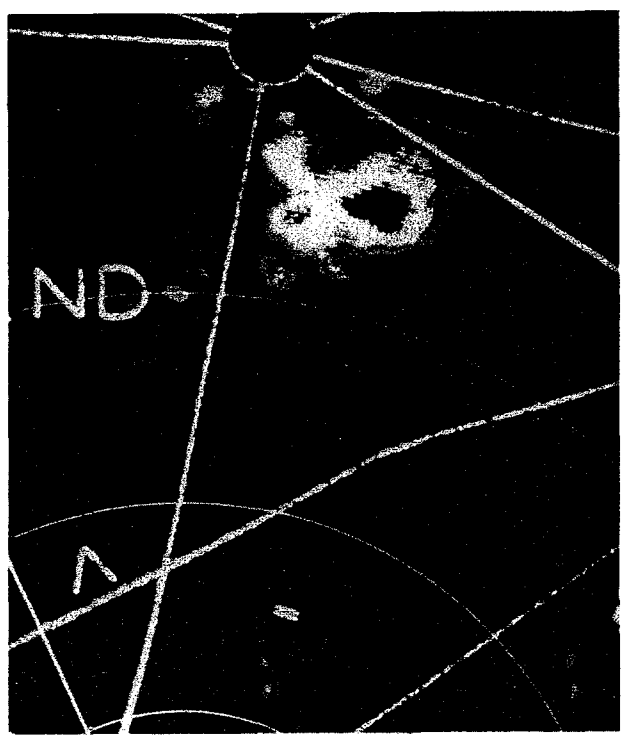

Figure 18. Control radar display, 19 June 1967.

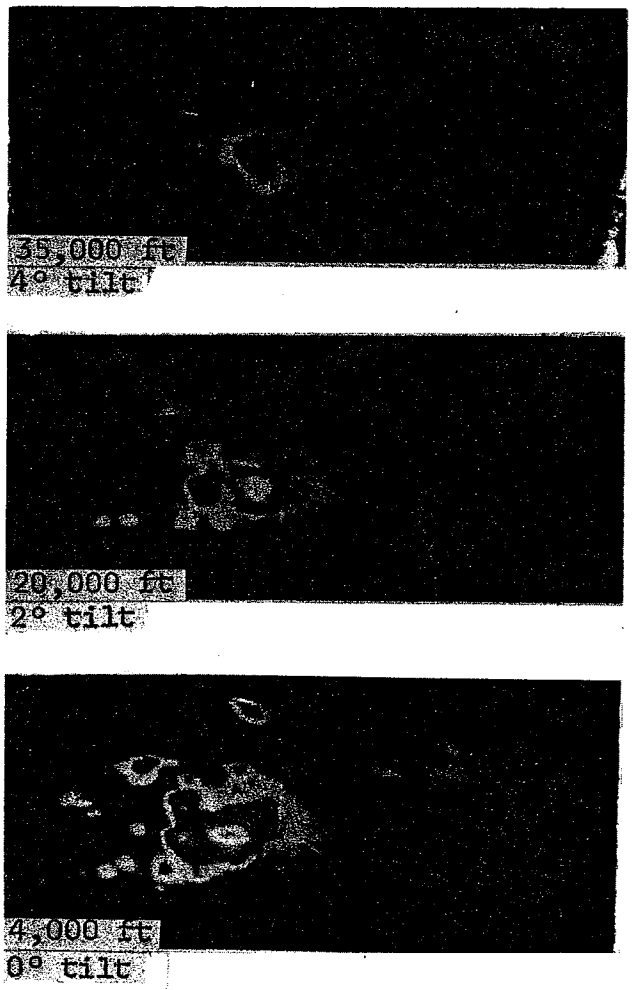

Figure 19. WSR-57 radar display at 0, 2, and 4° antenna tilt 19 June 1967.

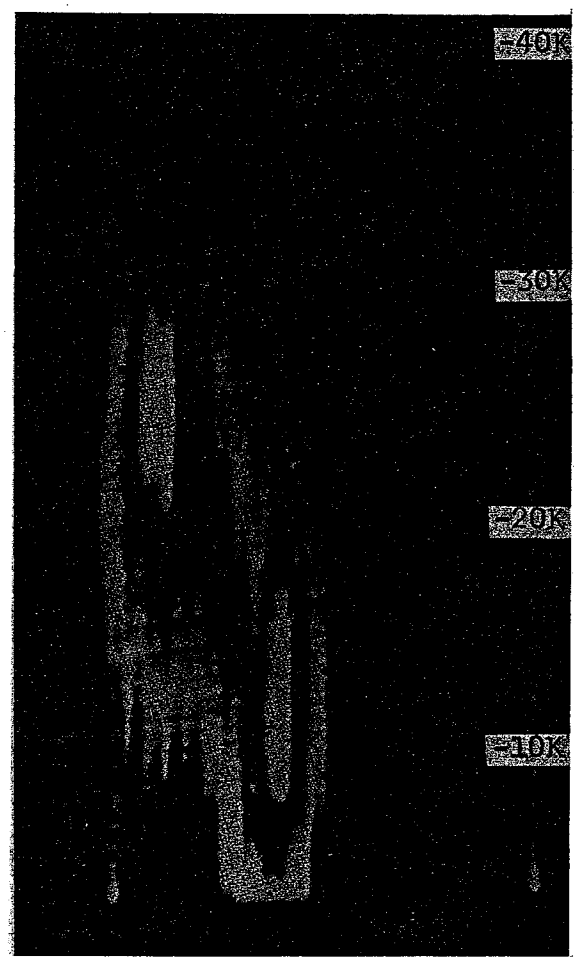

Figure 20. MPS-4, C-band height finder radar display, 19 June 1967.

than the maximum of $1 \times 10^4 mm^6 m^{-3}$ displayed by the air traffic control radar. As in the 21 June case, we suspect that the discrepancy arises from differences of antenna beam pattern and calibration uncertainties.

The MPS-4 C-band height-finder radar display in figure 20 show maximum reflectivities aloft. The ARSR-1D and WSR-57 radars with their wider beams may lose these maxima by vertical integration. However, the RHI profiles indicate that the beams of the airborne radars were sampling significant storm cross sections.

The P-38 flew the entire data run at 14,000 ft. Figure 21 shows the attenuation sequence started at 45 n mi from the storm. With no signal attenuation, the X-band radar shows a slightly larger echo with possible better definition. No significant precipitation attenuation is apparent. When approximately 10-db attenuation is applied to both receivers, the decrease in echo size is the same. However, note that

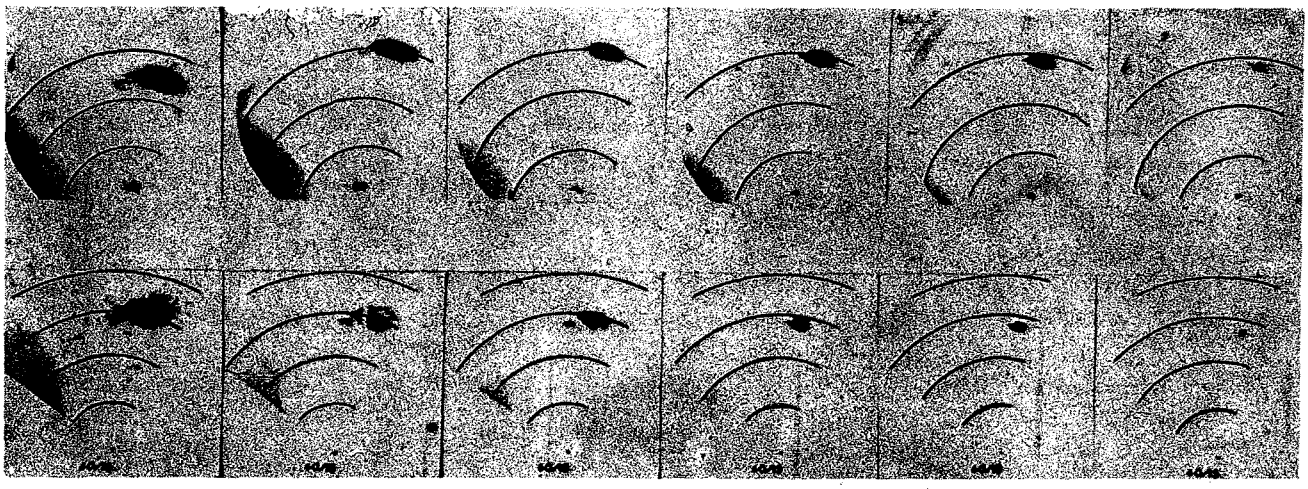

Figure 21. C-band (top) and X-band (bottom) radar step attenuation sequences, 19 June 1967. Range marks are 15 n mi.

the westernmost cell, shown best by the small cancellation (fig. 18) in the ARSR-1D display, is visible on the airborne X-band radar but not on the C-band radar. This is a combined result of slight differences in tilts of the two airborne antennas and the greater beam resolution of the X-band radar. The magnitudes of the equivalent reflectivity factor Z_e were calculated for the photographs showing equal storm areas. The areal cross sections of attenuation values of 16 to 18 db on the C-band and 21 to 22 db on the X-band radar match with the area of the bright core of the WSR-57 radar at flight altitude. The attenuation values were converted to Z_e by

$$Z_e = \frac{P_r R^2}{P_t C} , \qquad (3)$$

where P_r is the return power in watts, R is the range in nautical miles, P_t is the transmitter power in watts, and C is the radar constant, with a value of 1.83×10^{-17} for the C-band and of 8.2×10^{-17} for the X-band radar. The calculated Z_e values are then $1.35 \times 10^4 mm^6 m^{-3}$ for the C-band and $7.94 \times 10^3 mm^6 m^{-3}$ for the X-band radar. Since the corresponding Z_e for the WSR-57 is $6.3 \times 10^4 mm^6 m^{-3}$, the X-band and C-band radars measured storm intensities that differed by 2.5 db and were lower than the WSR-57 by 9 and 7 db, respectively.

The airborne values agreed closely with the air traffic control radar measurements which were between 4×10^3 and $7 \times 10^3 mm^6 m^{-3}$ for the same echo size.

The measurements of the two airborne radars agreed closely (± 3db), however, when the nineteen Z_e values of the airborne radars were compared with the WSR-57, the differences ranged from +2.8 to -16.3 db. The average difference was 6 db, with the WSR-57 measuring the higher reflectivity. The average distance at which the observations were made was 45 n mi. Figure 22 is a plot of the differences in the reflectivities measured by the WSR-57 and airborne radars for the runs on 19 June The average difference is about 6 db, an amount which depends also on the distance between the echoes and the WSR-57 radar, which was 70 mi. in this case. In most of the storms sampled, the WSR-57 range to the storm was approximately 70 n mi, twice as far as the aircraft. Notice that the estimates derived from the airborne radars tend to decrease with range relative to the WSR-57 estimates. If the pilot were able to control the elevation of the radar beam very accurately, he could illuminate lower intense portions of storms not visible from great ranges to the ground based systems. This would tend to offset the rapid degradation with range of airborne radar performance associated with their wide beamwidths.

7. COMMENTS ON THE COMPARISON OF THE ARSR-1D AND WSR-57 DISPLAYS AND THE DETECTION OF LIGHTNING BY THE ARSR-1D

The first comparative data for the WSR-57 and ARSR-1D radars were collected in the spring of 1964. An analysis was published as NSSL Technical Memorandum No. 1 (Wilk et al., 1965). In 1966, an NSSL signal processor was added to the ARSR-1D, and additional examples of

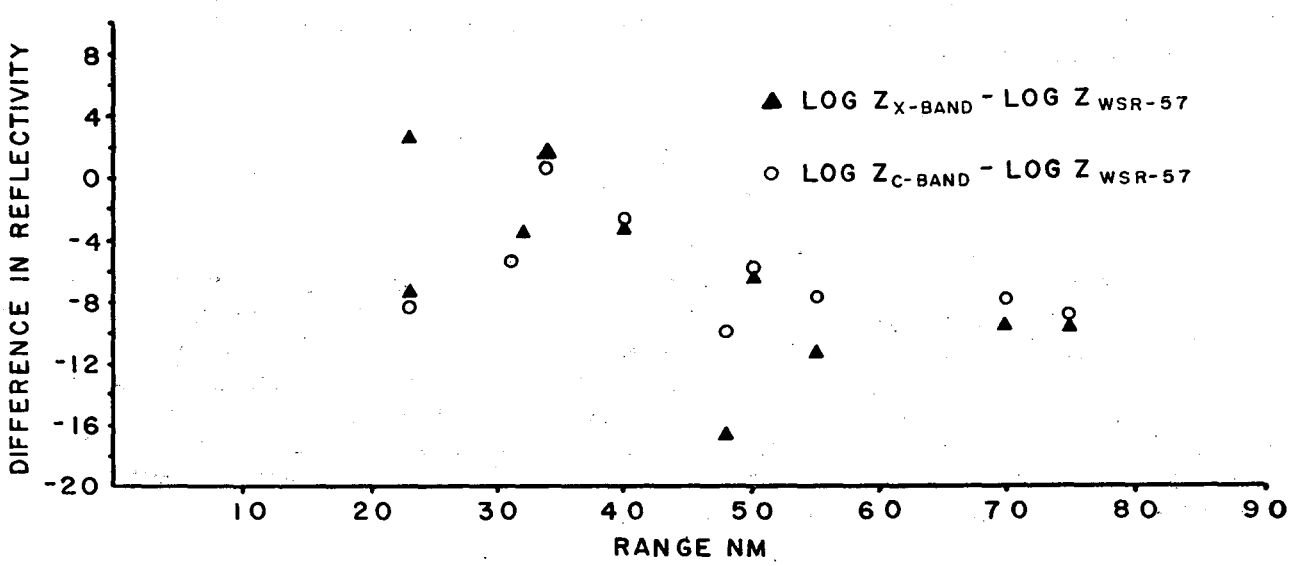

Figure 22. Ratios of C-band and X-band reflectivities to WSR-57 S-band reflectivities, 19 June 1967.

contour-mapped displays of thunderstorm activity were obtained. Because the ARSR-1D radar was used primarily for operational training at the FAA Academy, systematic calibrations were not possible, and the contours represented only rough approximations of reflectivities. As anticipated, however, the cell-by-cell match with the WSR-57 display was always good. The data of 20 May 1966 are included in this report to amplify the examples of the comparative displays discussed in other sections of this report.

A feature observed on the ARSR-1D, but not on the WSR-57, is the lightning echo. In figure 23, the arrow points to a nonprecipitation target frequently seen on the L-band radars. There is general agreement (Battan, 1959; Miles, 1952; Ligda, 1956; Atlas, 1958; and Hewitt, 1953) that this target is the ionized path associated with lightning. Under this assumption, Ligda (1956) calculated the electron density

Figure 23. ARSR-1D L-band control radar display, linear receiver, 3 April 1964. Lightning echo marched by arrow.

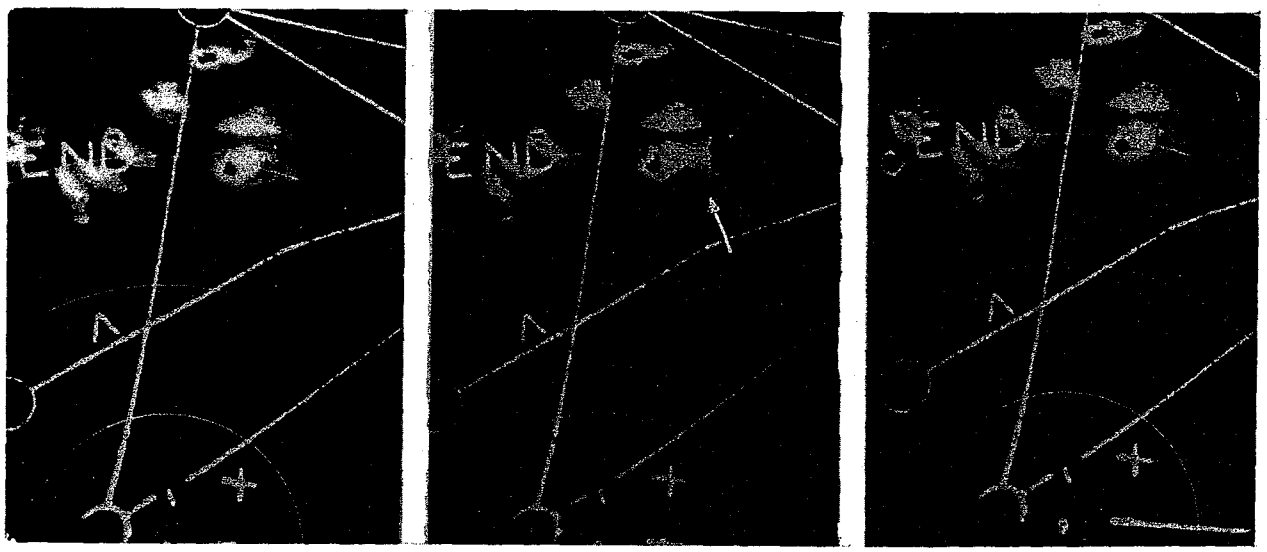

Figure 24. ARSR-1D L-band control radar integrated display log receiver, 20 May 1966. Arrow points to momentarily enhanced reflection discussed in the text.

necessary for detection by L-band radar as $2 \times 10^9 cm^{-3}$.* This is more than one million times less than the density of 10^7 reported to exist in lightning strokes (Uman and Orville, 1964). These ionized paths probably last about 0.3 sec (Miles, 1952), although the effective duration may be longer by a factor of 2 or 3 in charge centers within the cloud, where the channel termination is in corona discharge among the precipitation particles. Lengthy discharge paths (> 5 km) with a duration of the order of 0.5 to 1.0 sec will provide ARSR-1D radar targets of azimuthal coverage of 10 to 20°. However, the narrow cloud to ground channels probably do not provide the extensive echo shown; more likely, these are lower concentrations dispersed in the large charge centers.

Additional observations of lightning were recorded in 1965 with a signal processor on the ARSR-1D radar. Of the three sequential PPI photographs from this radar seen in figure 24, the center one shows a very unusual pattern. The clearest lightning echo is in the anvil cloud ahead of the thunderstorm. More interesting, however, is the extension of the moderate precipitation echo (shown by arrow), which shows that the ionization reflection is added to the precipitation signal, enhancing the total cross section. This suggests that processing of pulse amplitudes might provide information useful for the study of lightning targets within thunderstorm precipitation.

*A similar calculation discussed later in this section shows the critical value to be $2 \times 10^{10} cm^{-3}$. We assume that the table given by Battan (1959, p. 109) contains a typographical error and that all the values should be shifted by a factor of 10.

Although the scan rate is slower than desired for comprehensive observation of lightning, its potential for studying the properties of lightning echoes is high. According to Ligda (1956), the ARSR-1D radar meets two of the three requirements for lightning detection: It operates at L-band wavelength and has a horizontal half-power point beam width of 2°. The scan rate of 18° sec^{-1} is the most significant limiting factor. For optimum lightning detection the scan rate should probably be greater than 360°/sec, although additional research is needed to define this requirement in terms of sampling statistics.

The critical electron concentration for detection is loosely defined. The value mentioned earlier is defined by that concentration which sets the index of refraction, η, equal to zero. That is,

$$\eta^2 = 1 - \frac{Ne^2}{\pi m f^2} = 0 \ , \tag{4}$$

where f is the radar frequency, N is the electron concentration, e is the electron charge, and m is the electron mass.

If we assume $\frac{e^2}{m}$ is 2.54×10^8 in esu, and $\eta = 0$, then (4) reduces to

$$N = 1.24 \times 10^{-8} f^2 \ , \tag{5}$$

where N is the critical electron density, and f is the radar frequency in Mc sec^{-1}. There is little doubt that the ARSR-1D, operating at f = 1300 Mc sec^{-1}, will detect most, if not all, of the visible lightning if it is pointing toward it at the time of the flash. If the antenna is rotating at 3 rpm (18° sec^{-1}), and the recombination time in the major channels is taken to be 1.0 sec, then the radar is "listening" to the 18° sector 1/20th of the time. Analysis of the scope photos obtained during the storm of 20 May 1966 shows that 14 scans contained lightning echoes within a specific 18° sector for the 1-hour period from 2200 CST to 2300 CST. Six of the PPI displays are shown in figure 25. The expected true frequency is the product of the ratio of nonlistening to listening time (20 sec/1 sec), with the observed frequency equal to 280 occurrences per hour in this case. Also, since there were 120 radar scans during the hour and 14 contained lightning echoes, the percent of time the phenomena existed is the ratio 14/120 (100), or 12 percent.

Only three or four marginal lightning targets were found in the echoes outside the 18° sector. The data clearly show markedly greater activity in the hollow of the strong portion of the squall line, centered at 335° in the reference photographs.

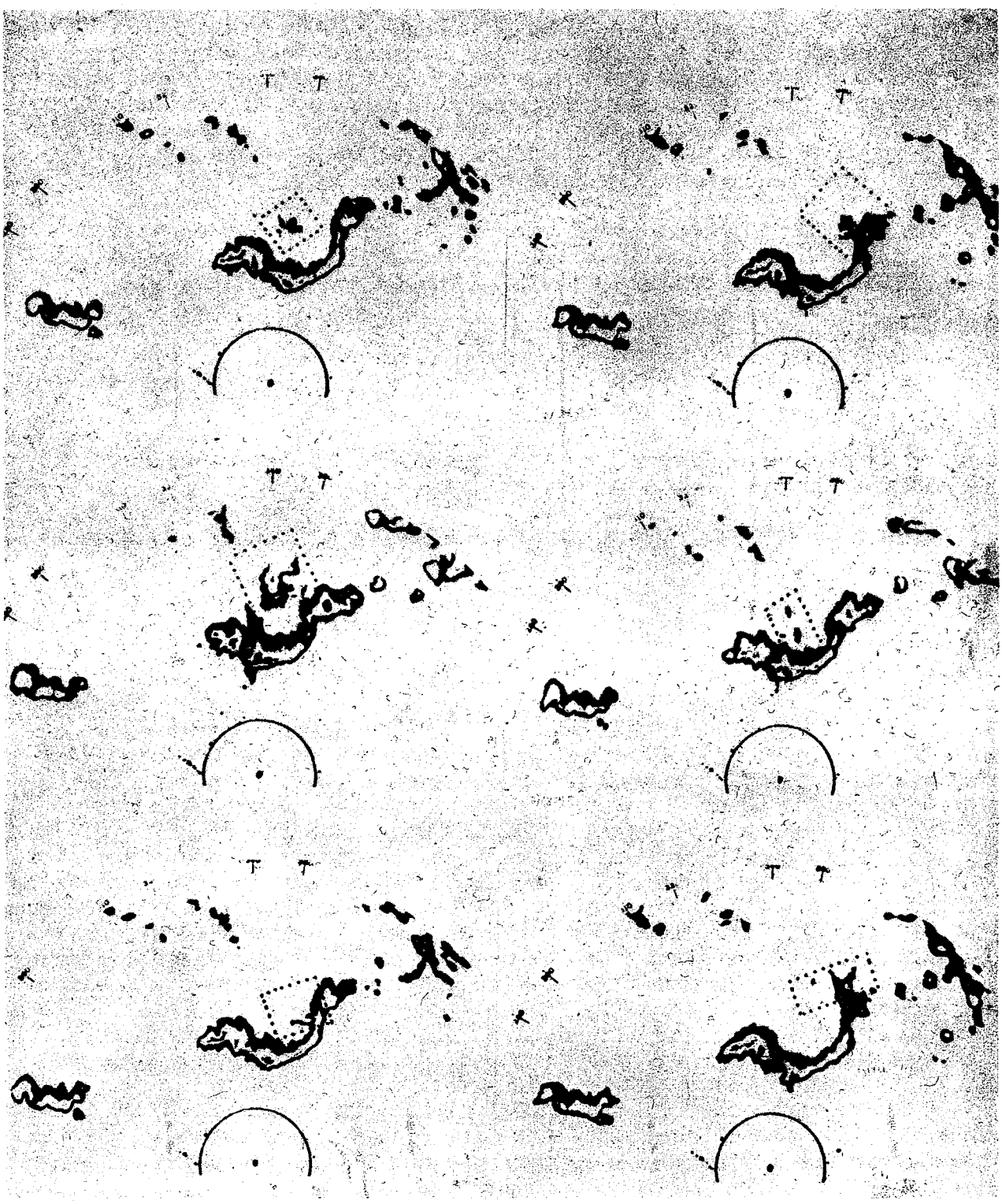

Figure 25. Examples of lightning displayed by the ARSR-1D radar, 20 May 1966. Lightning echo is enclosed in dotted box.

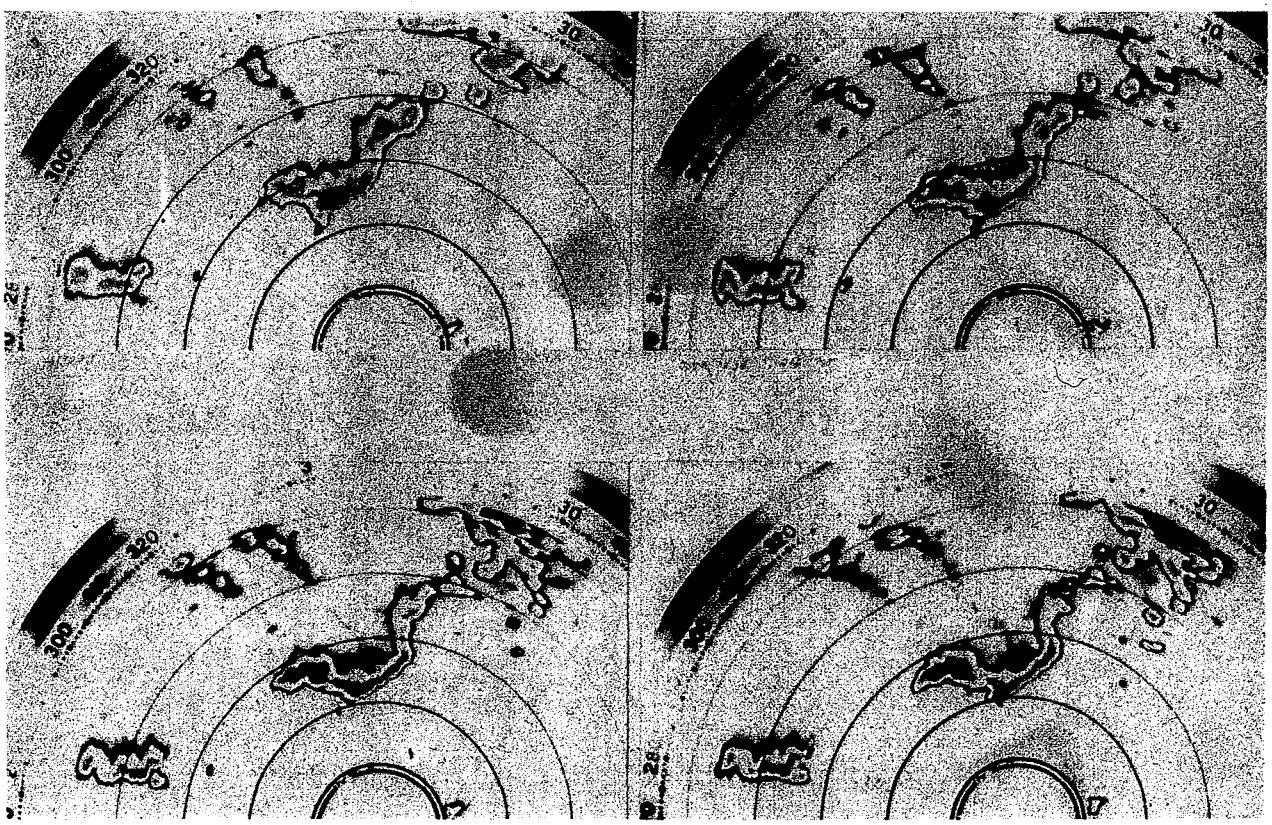

Figure 26. Examples of WSR-57 weather radar displays corresponding to the same time period as the ARSR-1D displays in figure 25.

The matching photographs from the WSR-57 radar are shown in figure 26. A study of the detailed features and collation of the convective centers in the comparative displays will answer most questions concerning the relative merits of the ARSR-1D and WSR-57 radar systems for thunderstorm detection. Large differences in the displays of echo structure are generally restricted to weak, stratified regions and do not raise questions concerning identification of the severe storms.

8. CASE STUDY - 30 APRIL 1967

The aircraft crews were alerted on 29 April for an expected flight at 1400 CDT on 30 April. By 1000 CDT on the 30th, the cold front expected to produce the thunderstorm activity was in central Oklahoma, as shown on the surface weather map in figure 27. A continuous line of convection developed shortly after 1200 CDT and moved eastward, exceeding the quantitative radar range (100 n mi) at approximately 1600 CDT.

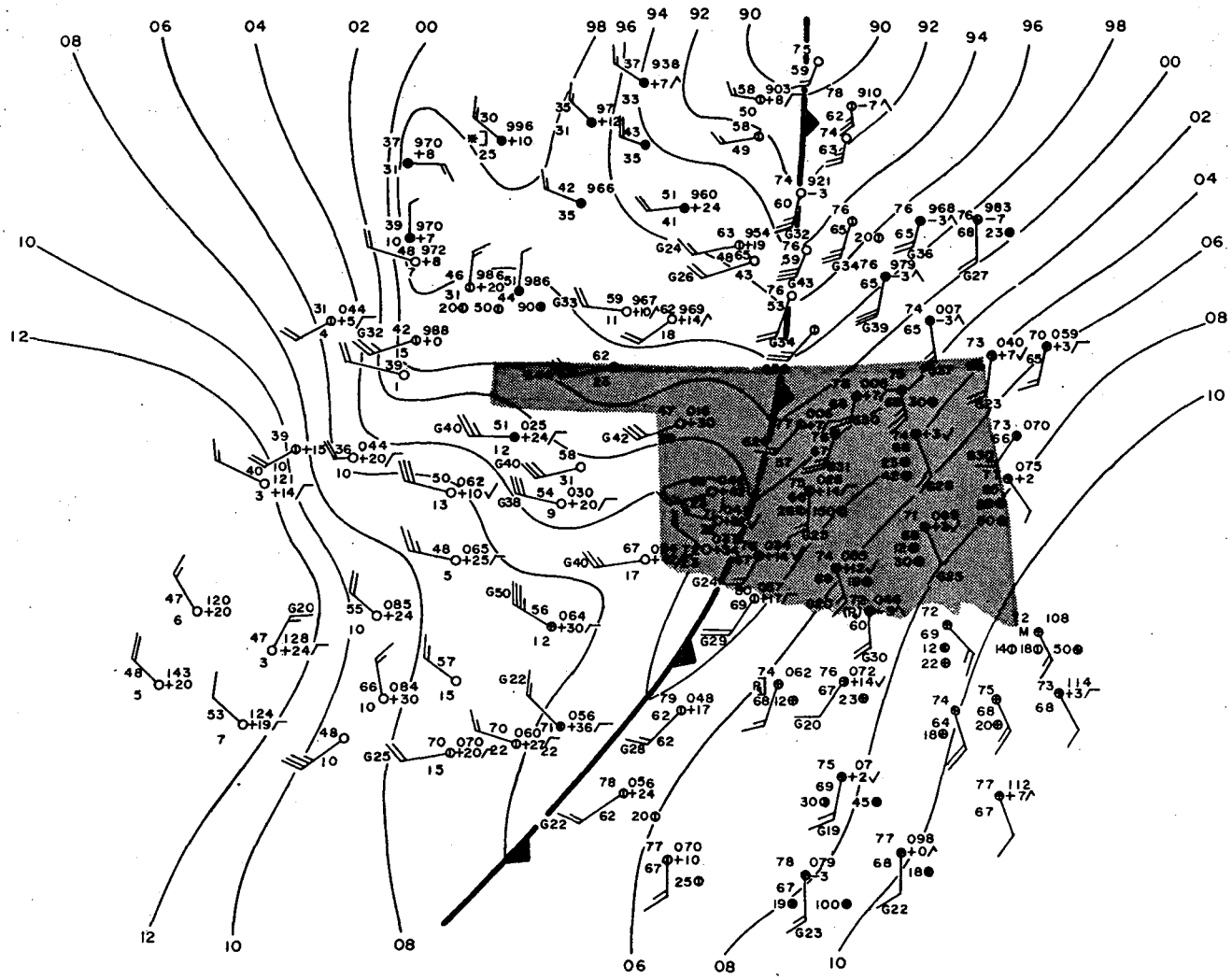

Figure 27. Synoptic surface chart for 0900 CST, 30 April 1967.

The P-38 aircraft arrived in Norman at noon but experienced radar camera trouble, and no data were collected. The RB-57 aircraft arrived at NSSL at 1511 CDT and made two approaches perpendicular to the squall line at altitudes of 33,000 and 30,000 ft, respectively.

At the time of the initial B-57 approach at 33,000 ft, the line of thunderstorms, located 80 n mi east of NSSL, was intense (log Z_e of max cores ≥ 5). The development of the convection is shown in the series of PPI displays in figures 28a through 28d. During the entire approach time, the most severe portion remained in the same geometric section of the line, with the intensity pattern remaining very stable for more than 2 hours. Such geometric stability in severe storm intensity patterns is not unusual in NSSL observations and appears to be the rule rather than the exception for large Oklahoma thunderstorms.

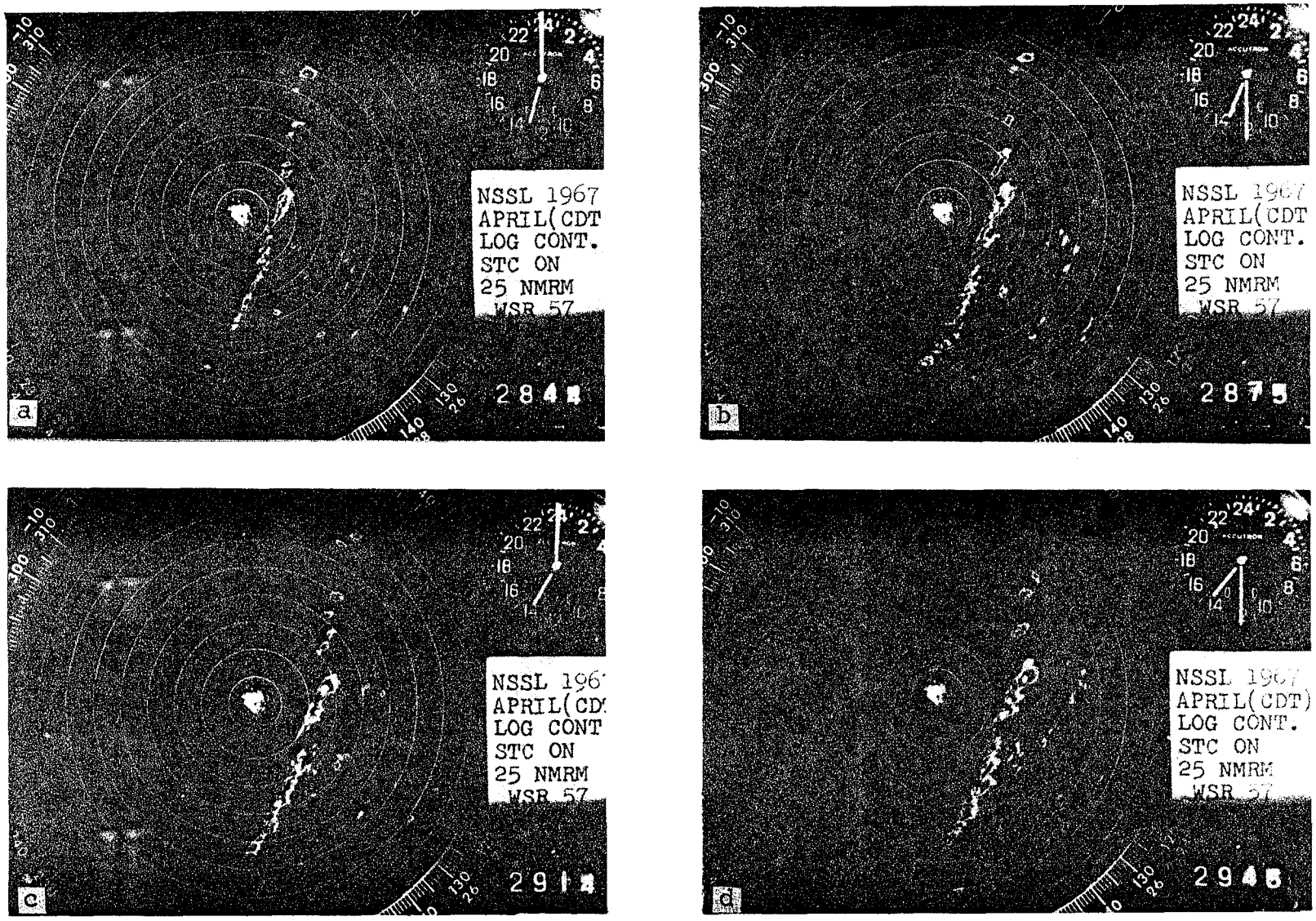

Figure 28. WSR-57 weather radar display of the development and movement of the squall line of 30 April 1967. The bright cores are ≥ $10^5 mm^6 m^{-3}$ and the range marks are 25 n mi.

An antenna tilt sequence (figs. 29, 30, 31) at 1405 CDT shows the line cross sections at radar beam interception heights of 2,000, 15,000, and 27,000 ft. The severe thunderstorm, which later produced hail and a tornado funnel cloud near McAlester, Oklahoma, was clearly visible at NSSL. A photograph taken at 1510 CDT (fig. 32) shows the distinctive Pileus cap (behind the radar tower), which corresponds with the intensity maximum of the PPI picture in figure 29. An RHI photograph (fig. 33) taken during the development of the southernmost cap at 1417 CDT places the maximum storm top at approximately 55,000 ft. A sample of the hail that fell at 1420 CDT is shown in figure 34.

This same portion of the squall line was first seen by the B-57 crew at a range of 150 n mi, but it did not appear on the radar until the range had decreased to 90 n mi. However, the first PPI displays (fig. 35) show a relatively strong signal at 90 n mi, indicating that initial detection should have occurred at a greater range. Since the antenna tilt is very critical (Merritt, 1967), weak signals may go undetected if the radar beam is not properly oriented with respect to the storm core, reducing the radar's effective range significantly.

On the first approach, the B-57 flew directly over the Oklahoma City VOR on a course nearly perpendicular to the squall line. The track of the aircraft, obtained from a composite of CPN-18 air traffic control radar photographs, is shown in figure 36. The severe thunderstorm echo is easily discernible even with this relatively insensitive ATC radar (fig. 37).

The K_a-band radar operator scanned the storm in the PPI mode during the next 30 n mi of the approach. At 1510 CDT the aircraft was 70 n mi from the squall line, and the radar display showed three areas of convection (see fig. 38). These correspond to the areas similarly marked on the WSR-57 radar display in figure 39. A fourth area shown on the WSR-57 PPI is absent on the K_a-band scope and presumed to be completely attenuated by the very intense precipitation in the primary thunderstorm core (echo 1).

The early detection advantage provided by high aircraft altitude may be somewhat offset when a storm beyond the earth's horizon is viewed through a nearer storm. Then, the radar beam may look at the secondary cell through a lower intense region of the primary cell. The fourth cell described above, which was apparently completely attenuated at K_a-band, is a good example of the radar beam-echo aspect problem in measuring representative storm intensity values (Merritt, 1967). The calculated attenuation through the nearer core is greater than 70 db, but less than 100 db, and depends upon approach angle.

At 1515 CDT (fig. 40) the K_a-band radar operator changed the range from 100 to 50 n mi. Attenuation lobes then became visible on the far side of echo number 1, and the operator switched to an RHI scan mode

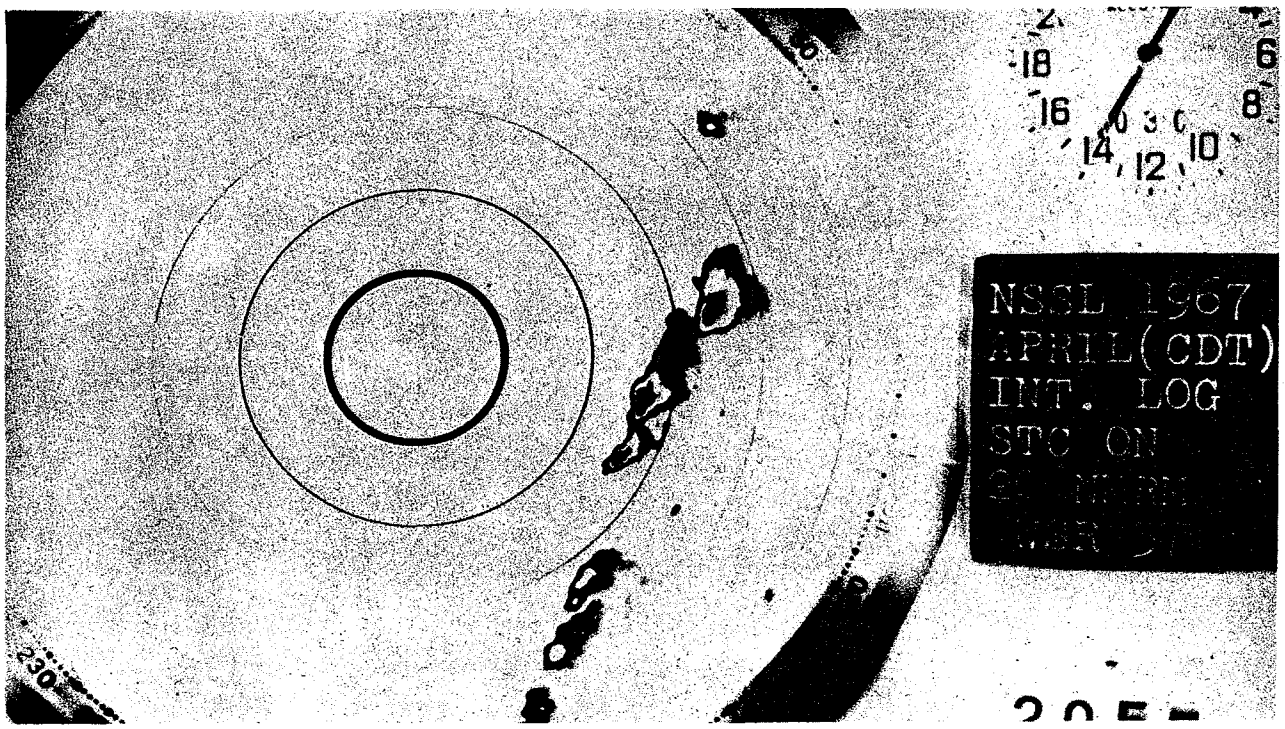

Figure 29. WSR-57 radar integrated video display. Core values are $10^4 mm^6 m^{-3}$. Mean beam height is 2,000 ft.

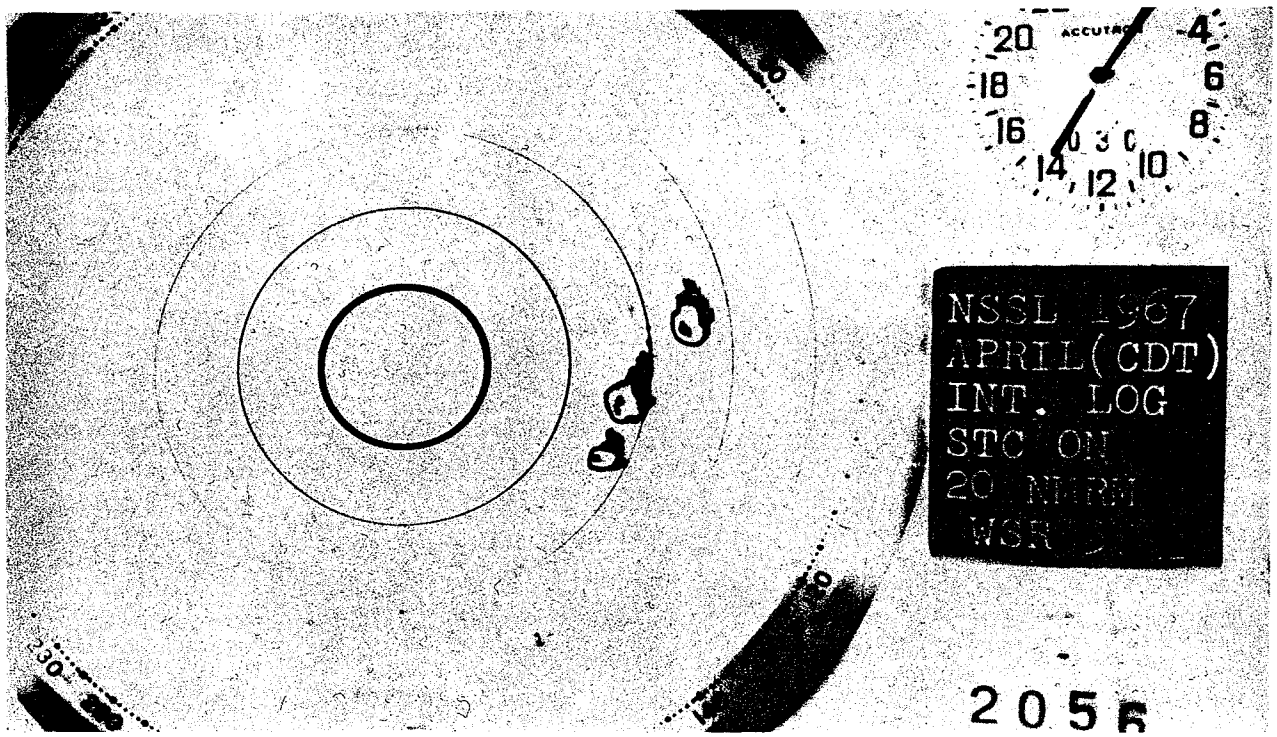

Figure 30. WSR-57 radar integrated video display. Core values are $10^4 mm^6 m^{-3}$, and mean beam height is 15,000 ft.

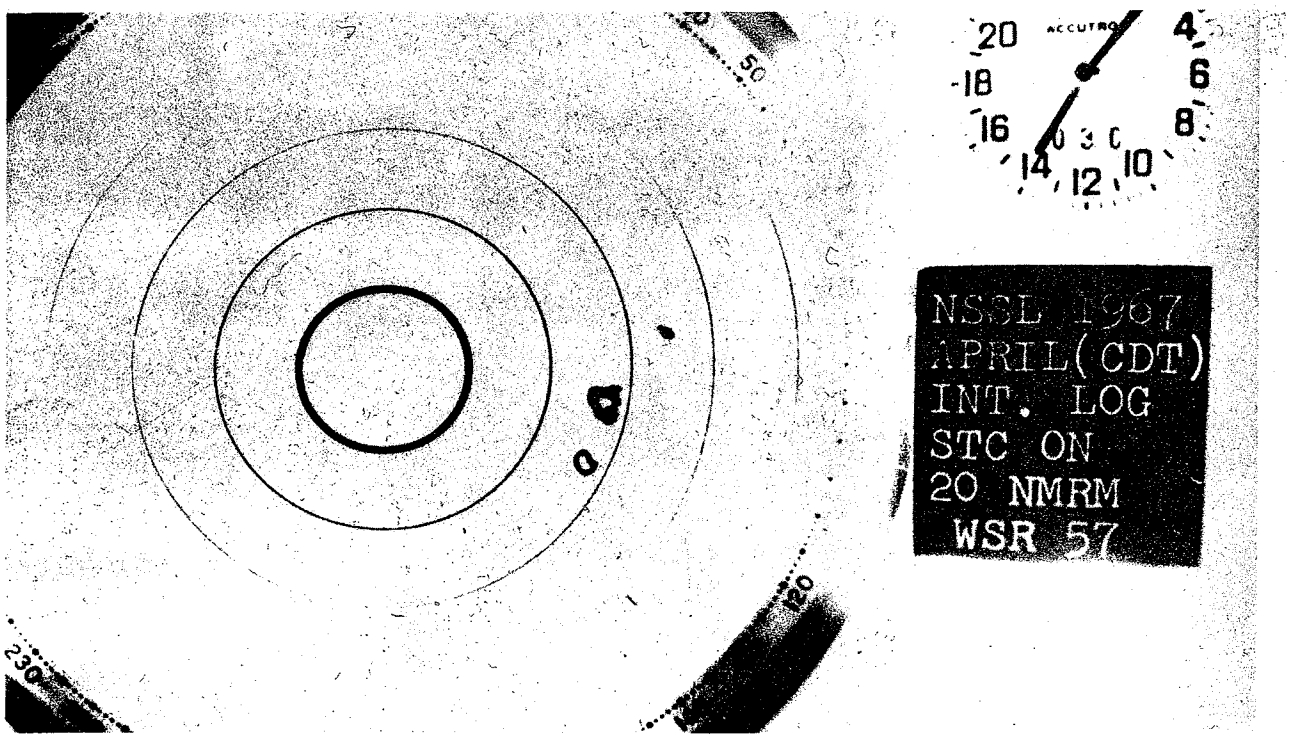

Figure 31. WSR-57 radar integrated video display. Cancellation is $10^3 mm^6 m^{-3}$ and mean beam height is 27,000 ft.

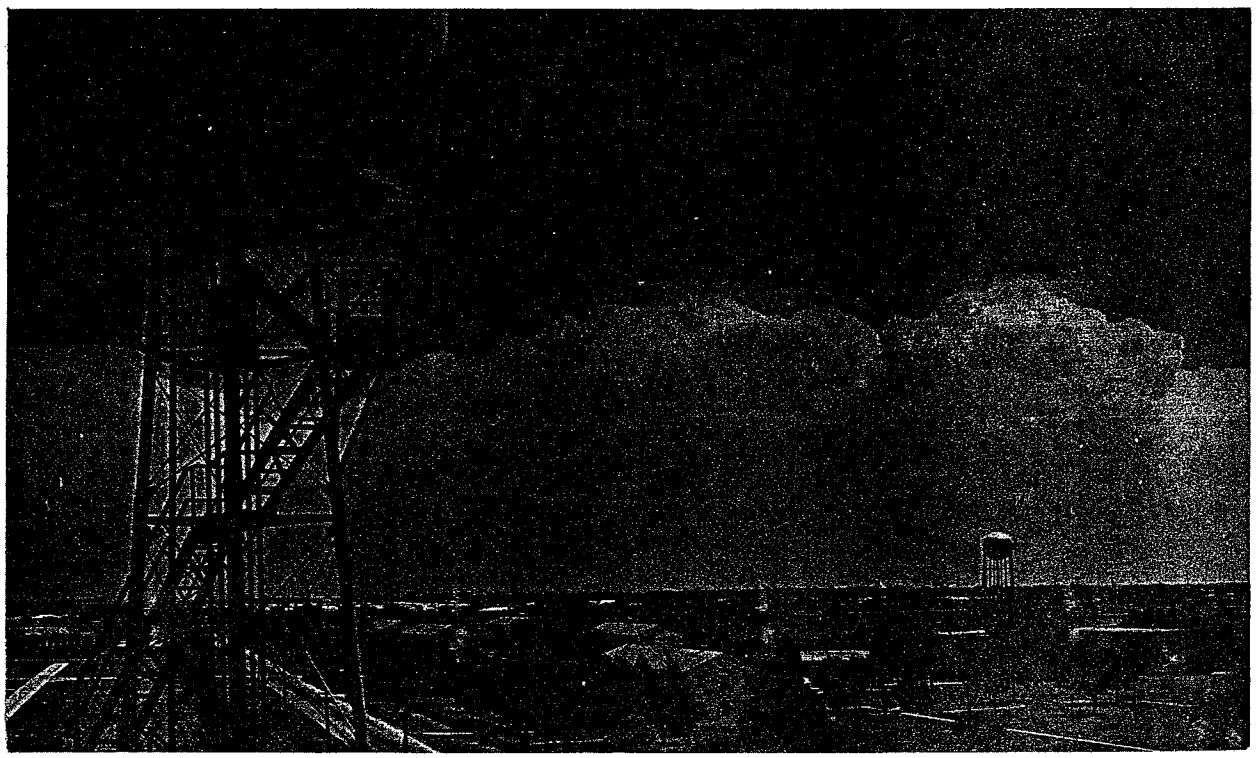

Figure 32. Squall line as viewed from NSSL, 1510 CDT, 30 April 1967.

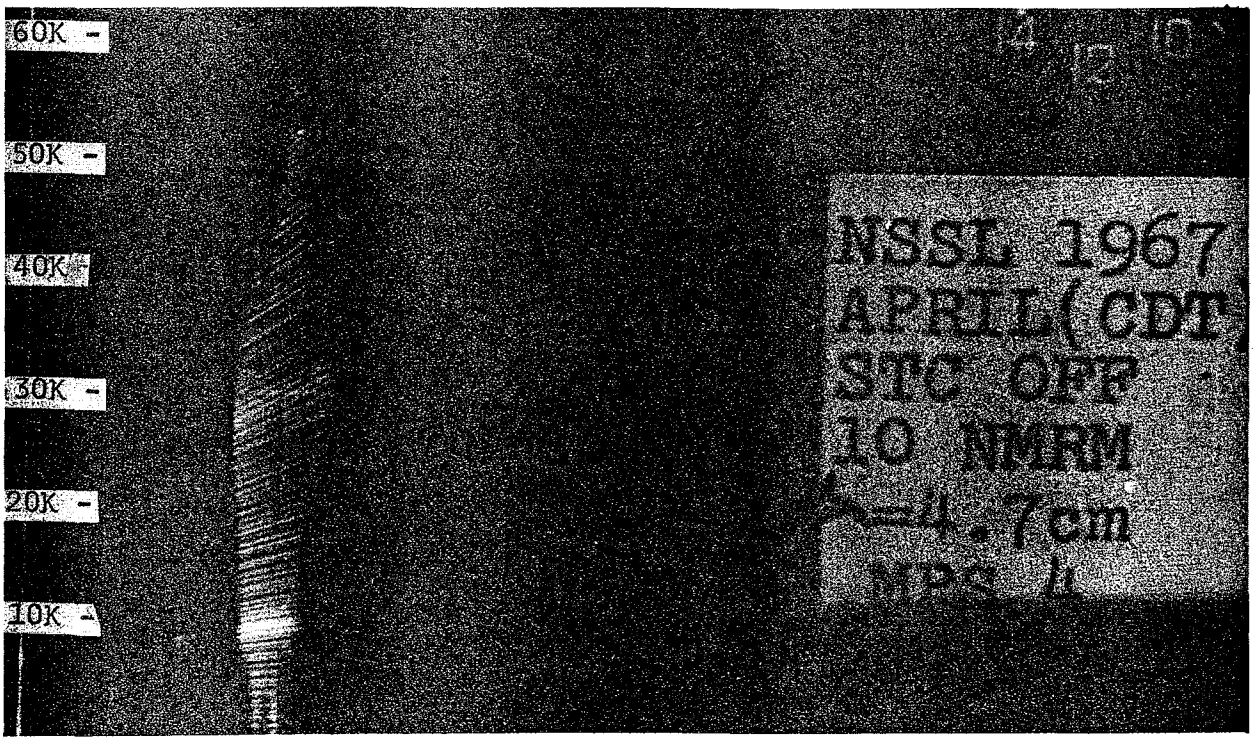

Figure 33. MPS-4 height-finder radar display of the severe thunderstorm of 30 April 1967 at 1417 CDT.

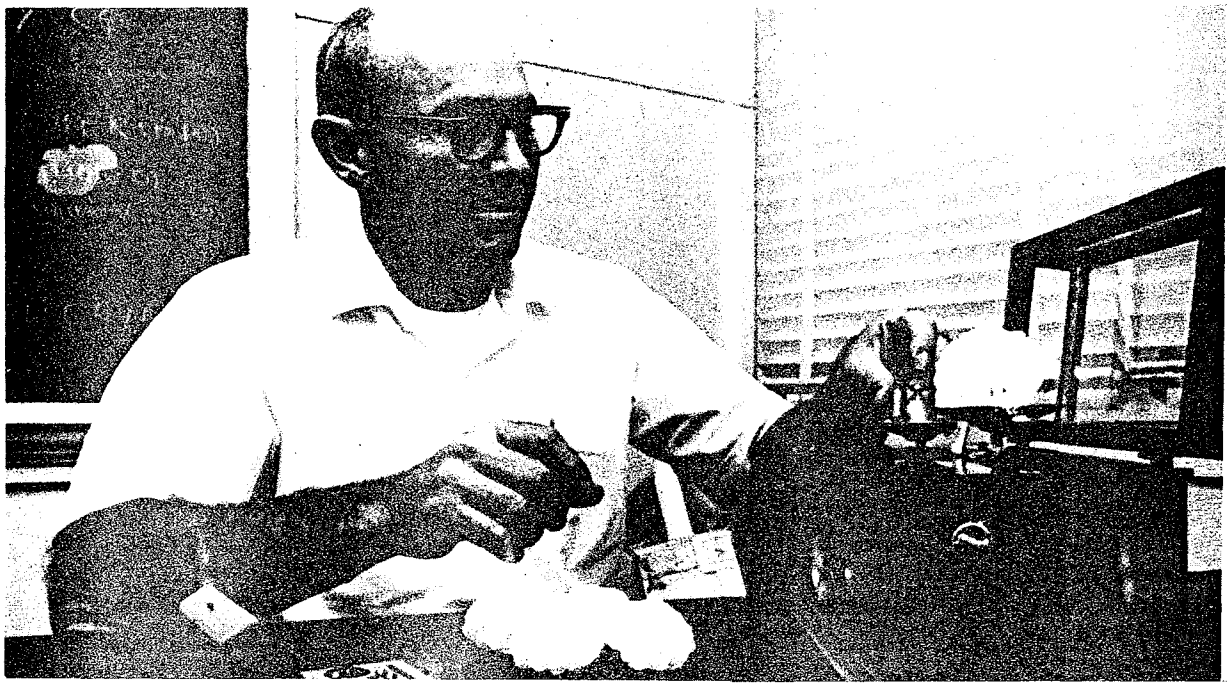

Figure 34. Samples of hail from the severe thunderstorm at 1420 CDT.

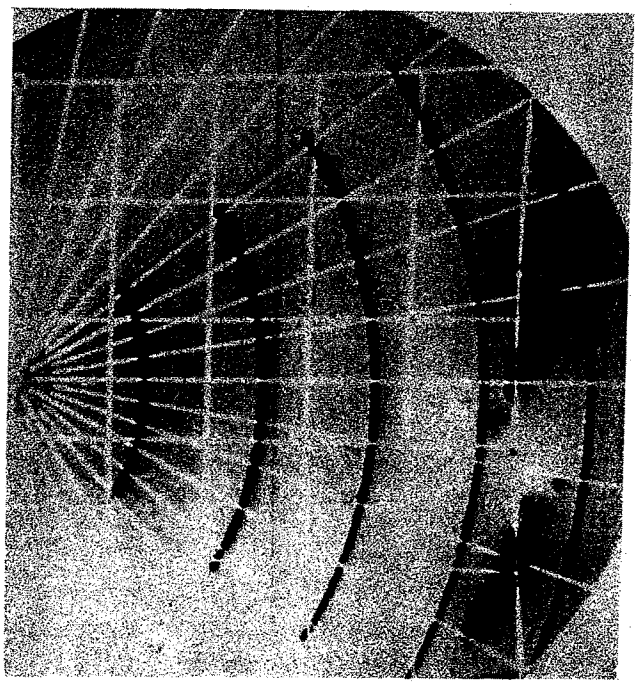

Figure 35. (left) K_a-band airborne radar display at 1410 CST. Range marks are 20 n mi.

Figure 36. (below) B-57 (K_a-band radar) track acquired with NSSL CPN-18 radar. The first pass ends at 1420 CST, and the second pass begins at 1427 CST, descending to 20,000 ft.

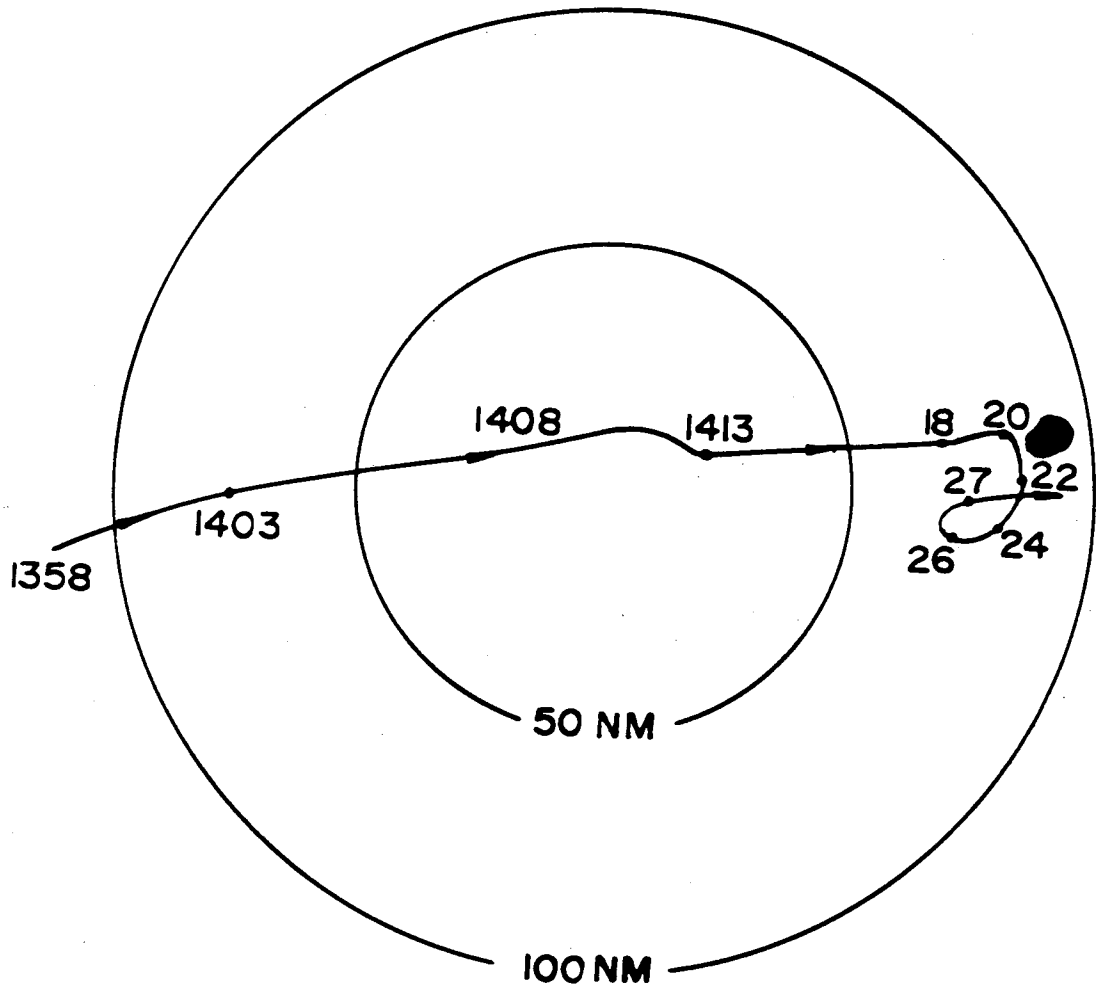

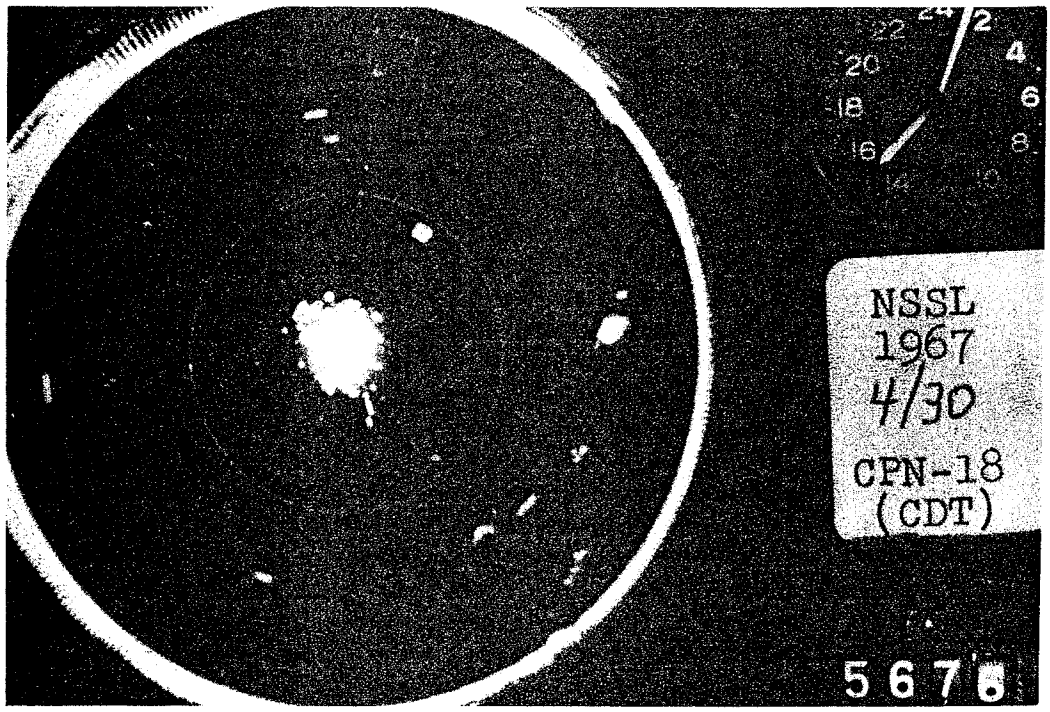

Figure 37. NSSL CPN-18 control radar display, 30 April 1967.

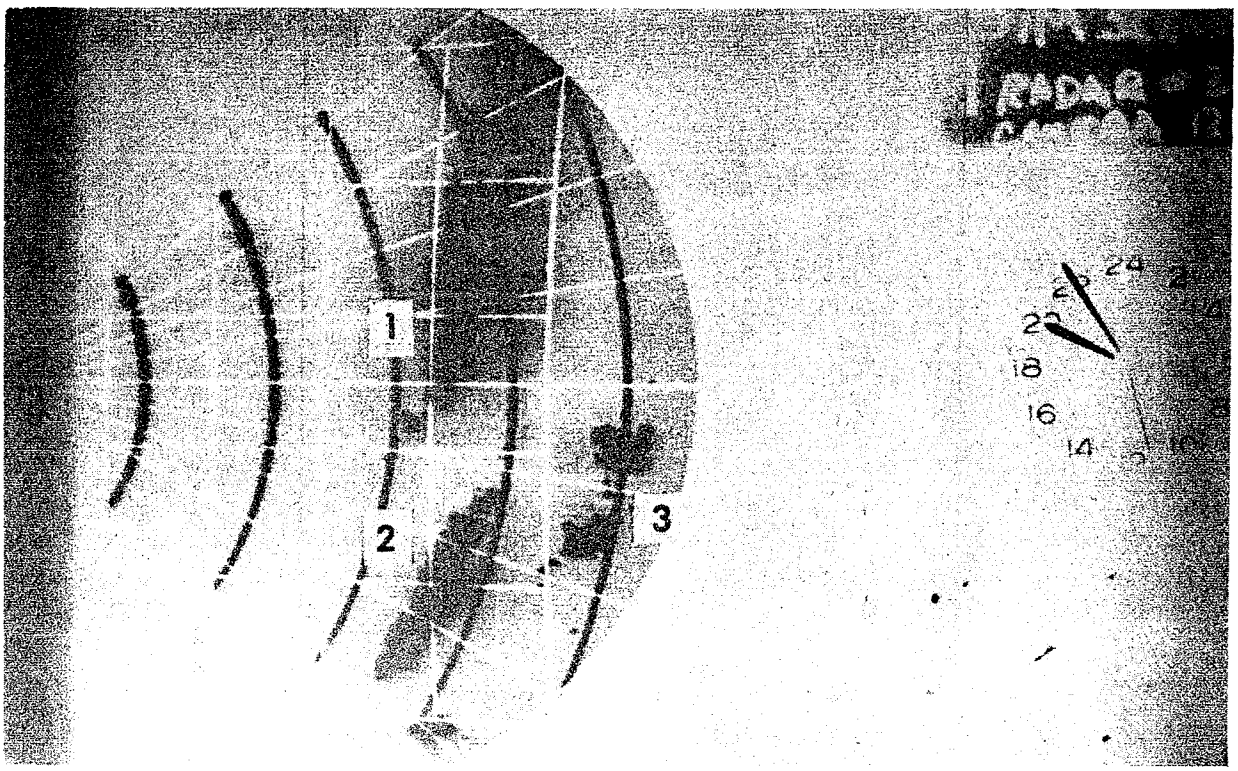

Figure 38. K_a-band airborne radar display. Range marks are 20 n mi.

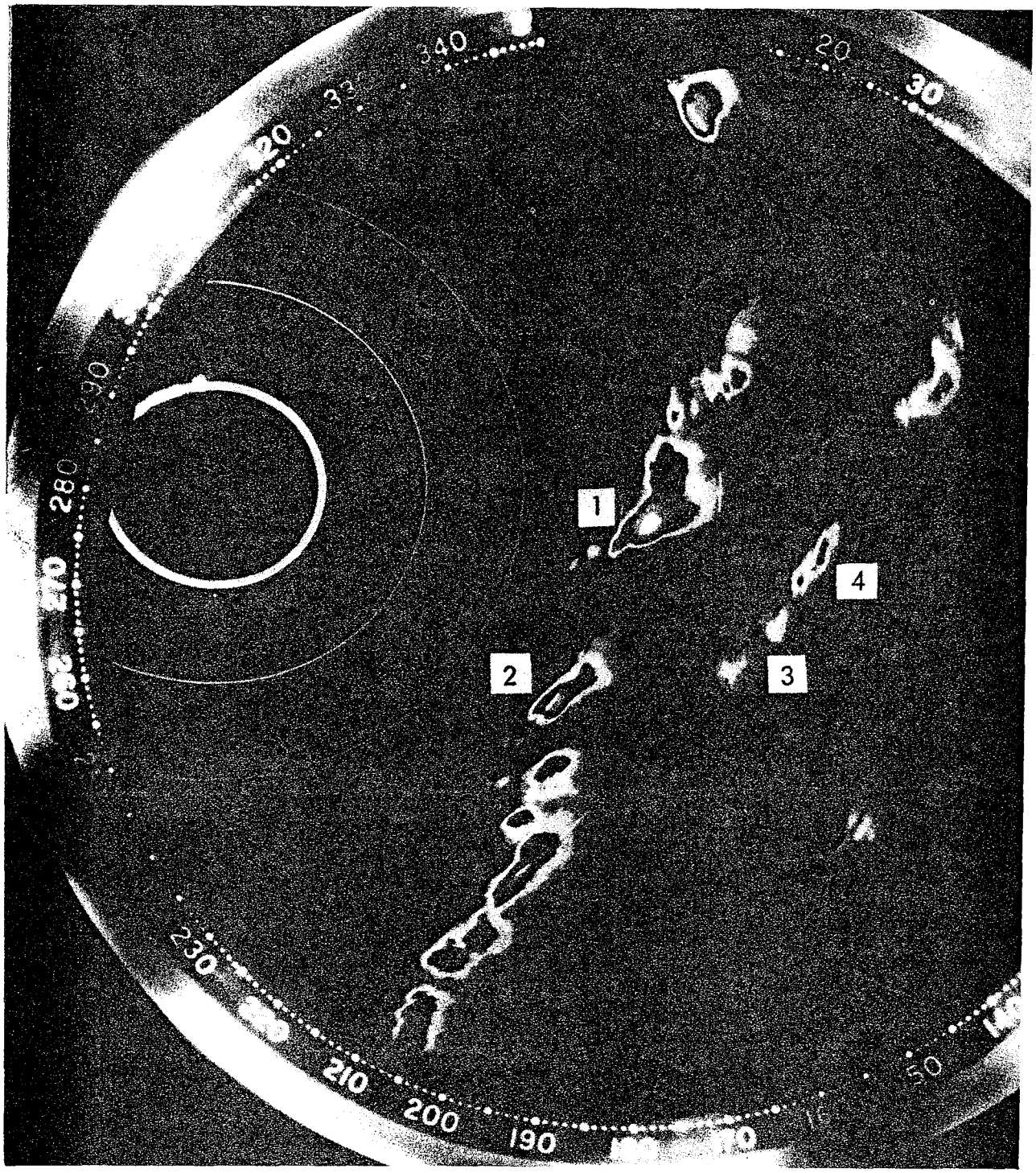

Figure 39. WSR-57 weather radar integrated video display. Range marks are 20 n mi. Bright core in echo no. 1 corresponds to $\geq 10^5 mm^6 m^{-3}$.

and recorded the displays shown in figure 41. The top of the precipitation echo appears at approximately 50,000 ft, which agrees well with the earlier ground radar measurements. After a 2-min RHI scan, the operator returned to the PPI mode, with the radar range set to display 0 to 25 n mi. Simultaneous, uncalibrated contour mapping during these PPI scans produced cancelled video of the southwest quadrant of the thunderstorm, as seen in figure 42.

Considering the difference in perspective, the display in figure 42 shows some agreement with the WSR-57 radar contour mapping in figure 43. The photo of the ground radar display taken 15 minutes later (1535 CDT, fig. 44) illustrates the change taking place in the convective structure of the storm. On close examination of echo number 1 in figures 43 and 44, one might attribute the changing convective structure

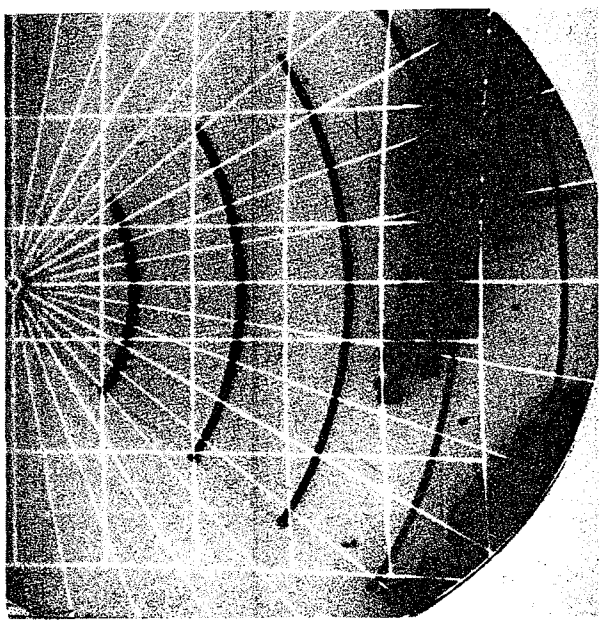

Figure 40. (left) K_a-band radar display. Range marks are 10 n mi.

Figure 41. (below) K_a-band radar RHI display. Overlay vertical lines are 10 n mi range marks.

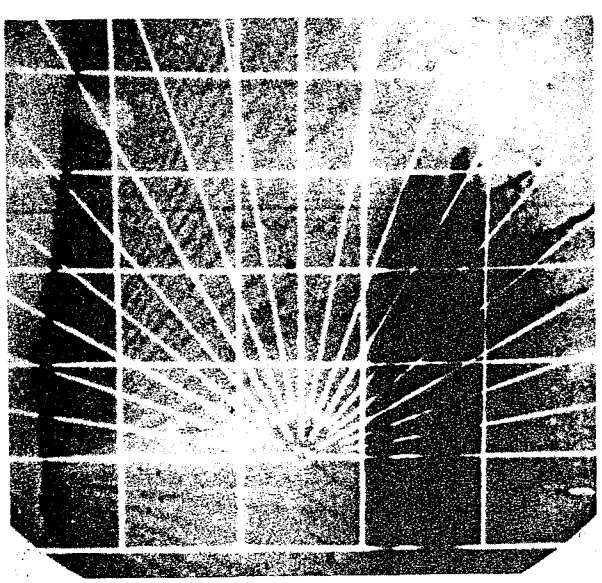

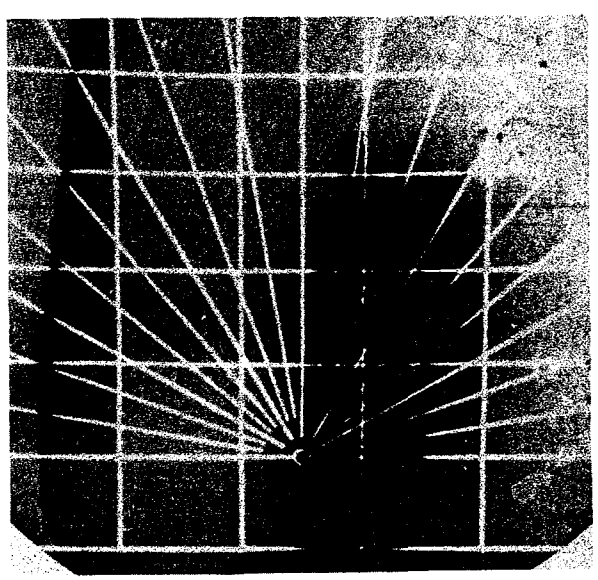

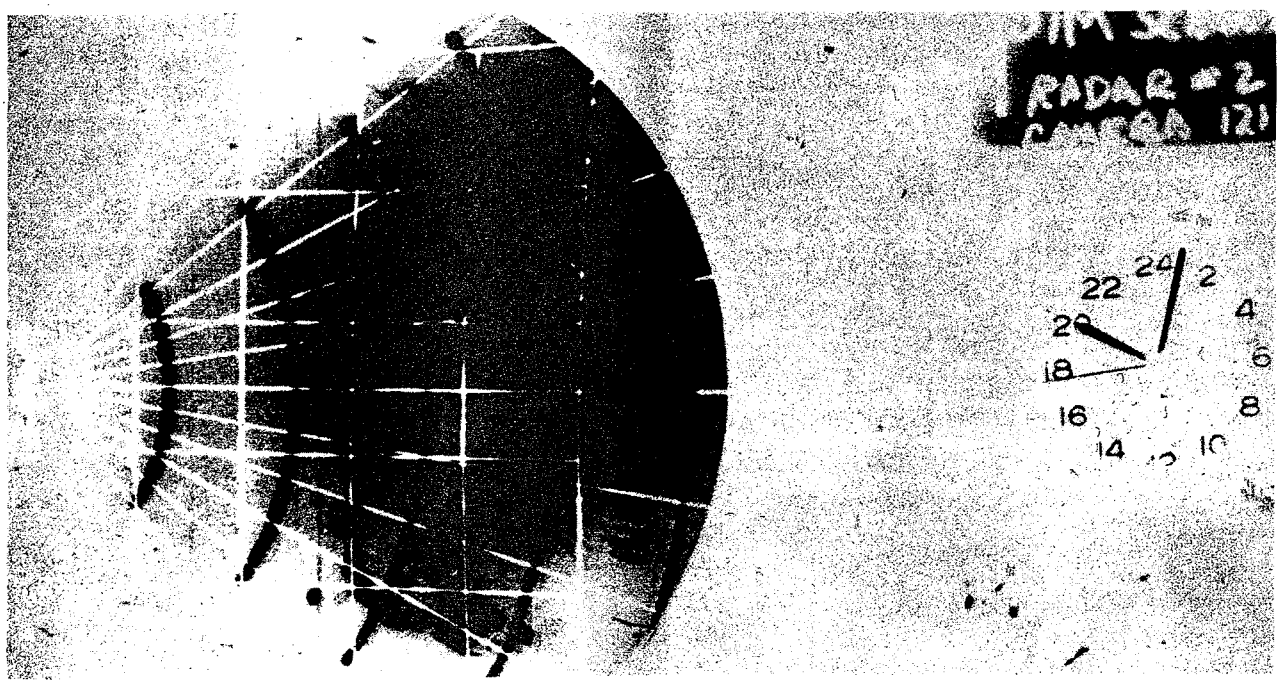

Figure 42. K_a-band radar PPI display with iso-echo contour. Range marks are 10 n mi.

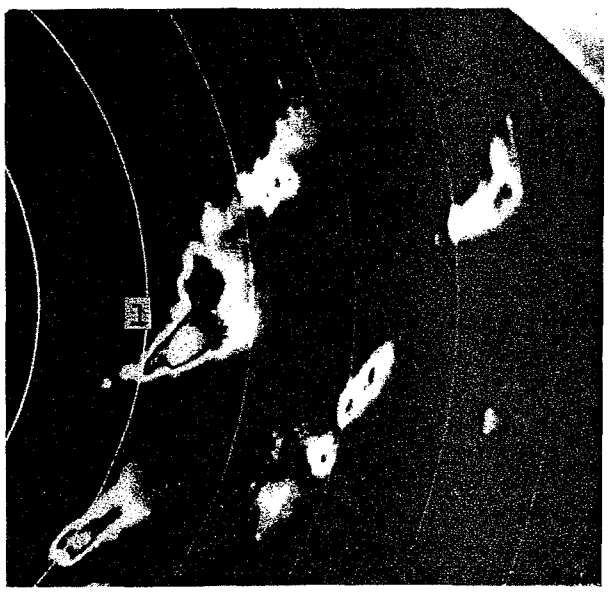

Figure 43. WSR-57 radar integrated video display corresponding to K_a-band photograph in fig. 42. Range marks are 20 n mi.

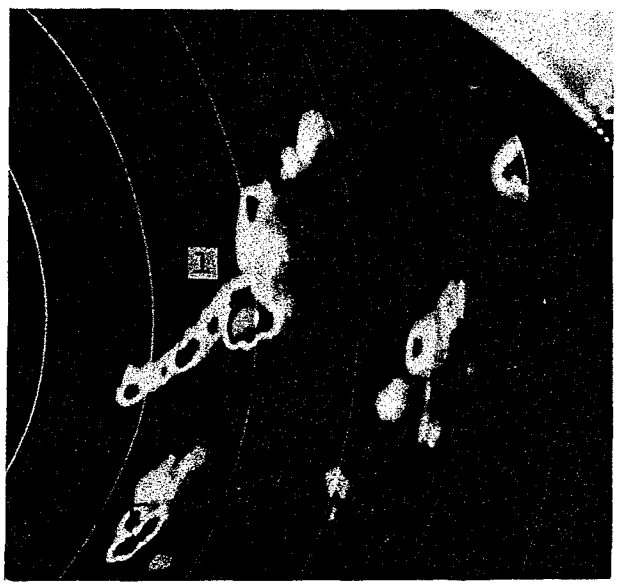

Figure 44. WSR-57 radar integrated video, 15 minutes after the display in fig. 43. Range marks are 20 n mi.

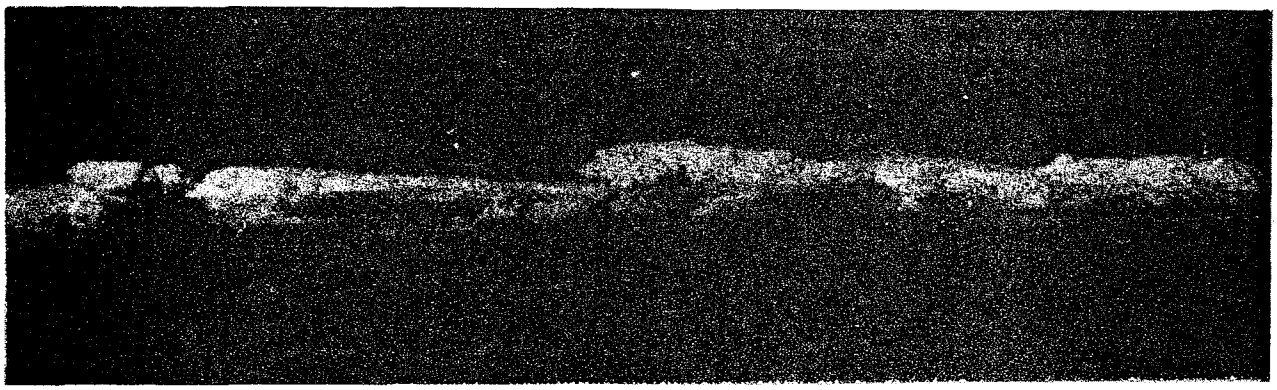

Figure 45a.

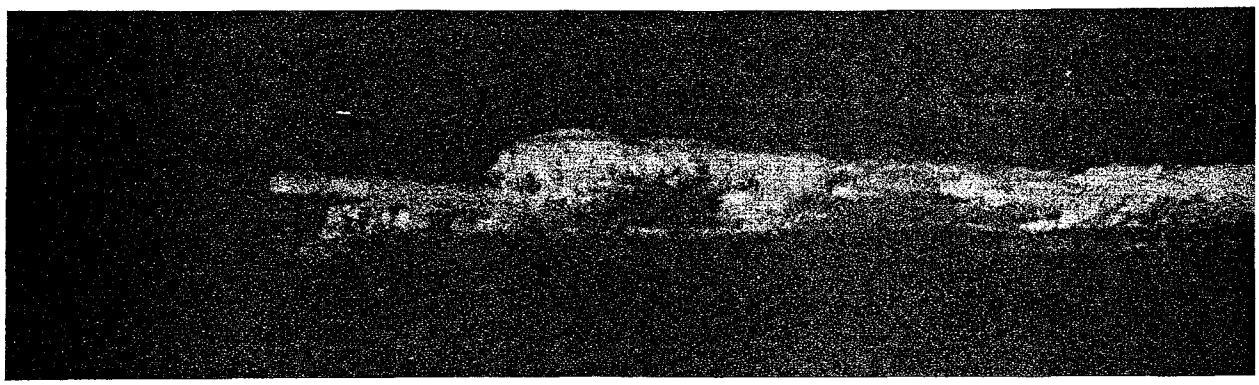

Figure 45b

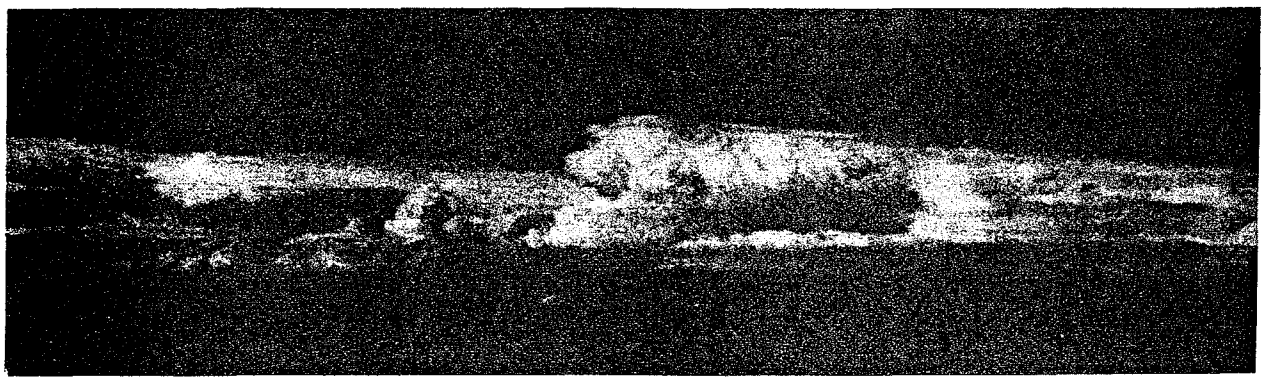

Figure 45c

Figure 45. Wing camera approach views of squall line, start range is 90 n mi in fig. 45a. Total time of sequence is 17 min shown in figs. 45a through 45h. Further discussion is given on p. 43.

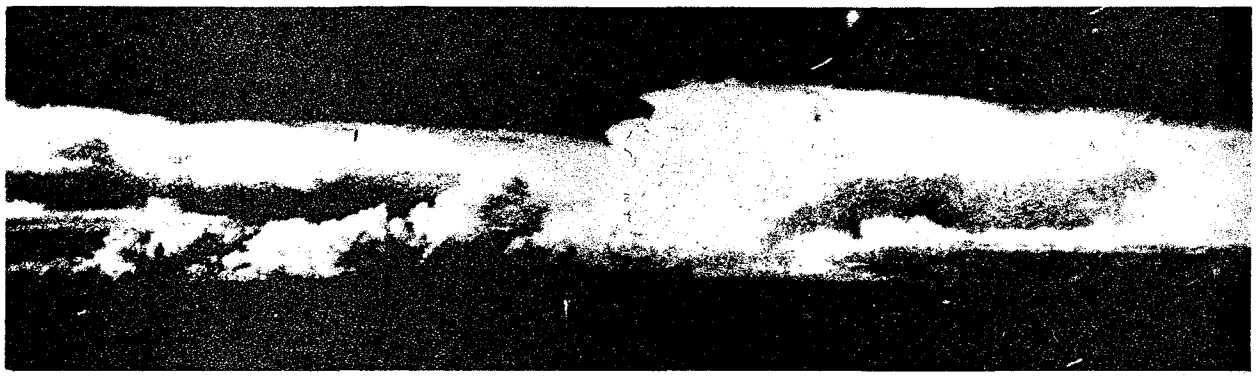

Figure 45d

Figure 45e

Figure 45f

Figure 45g

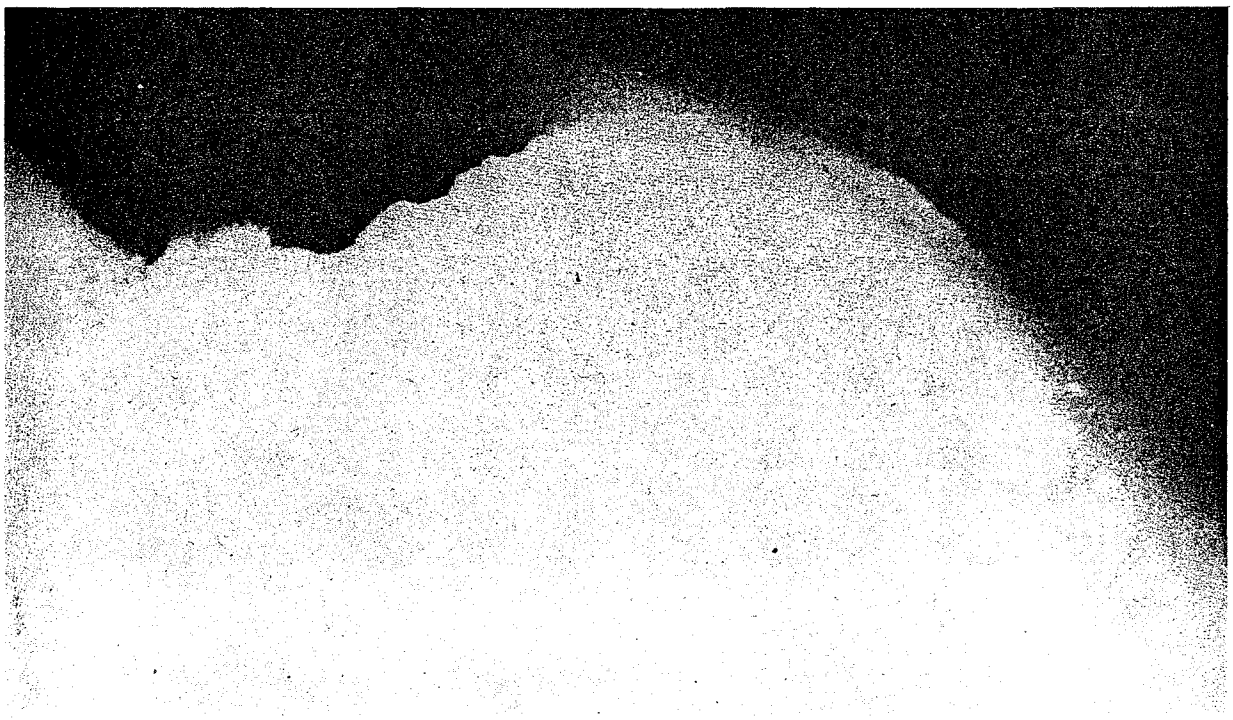

Figure 45h

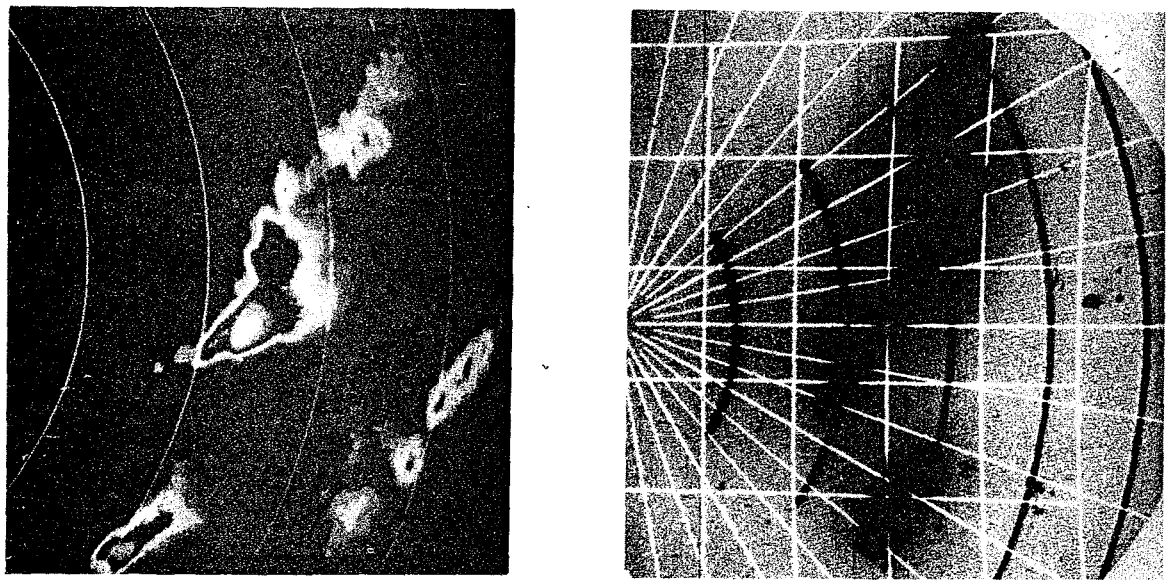

(a) (b)

Figure 46. WSR-57 (a) and K_a-band (b) PPI displays. Range marks are 20 n mi.

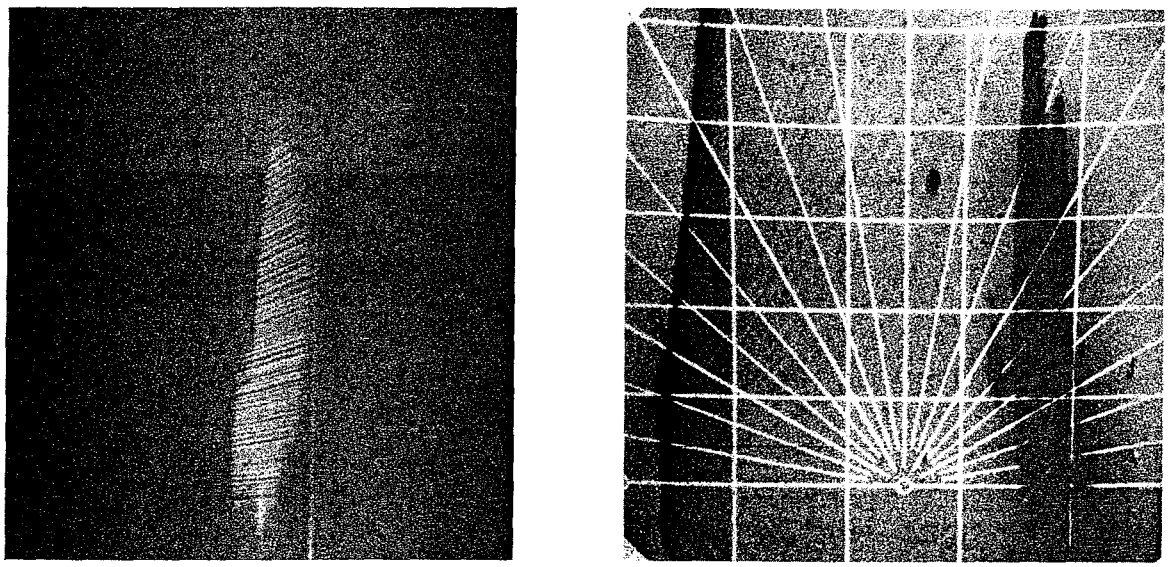

(a) (b)

Figure 47. MPS-4 (a) and K_a-band (b) RHI displays. Tops of both echoes are approximately 45,000 ft. The aircraft altitude is 20,000 ft, and the horizontal overlay lines are 5,000-ft interval markers.

to an intensified counterclockwise circulation. This conjecture is strengthened by confirmed reports of sightings of tornado funnel clouds, which are believed to develop with such circulation patterns.

Figures 45a through 45h show the aircraft's initial approach as seen by the 35-mm wing camera. Figure 45a was taken at approximately 1403 CST about 90 n mi from the storm. Figure 45h completes the approach sequence at 1420 CST at a range of about 3 mi, with the aircraft banking to the right. The PPI and RHI pictures in figures 40 and 41 correspond in time to the wing camera photos of figures 45b and 45g.

As seen in figure 36, the second pass consisted of a hook pattern, with the aircraft descending to 20,000 ft. Figures 46a and 46b show good correlation in echo geometry between the time-matched PPI scans of the WSR-57 and K_a-band aircraft radars during this second approach. Figure 47a shows the aircraft PPI display near the end of the second pass. Figure 47b shows the correlation between the NSSL MPS-4 RHI radar and the aircraft radar in the RHI mode at a time between that of figures 46b and 47a.

During both passes, the K_a-band radar provided an adequate qualitative three-dimensional description of the severe thunderstorm. Attenuation caused minor signal losses and reduced the signal power returned from weak to moderate showers to a level below radar detectability in the shadow of the severe thunderstorms. In general, attenuation reduced the average echo depth by about 25 percent. The K_a-band radar may not be adequate for approaches other than perpendicular to a squall line, and only a carefully designed large-scale flight program could yield the statistical information necessary for evaluating K_a-band performance for severe weather detection.

9. CASE STUDY - 5 MAY 1967

The aircraft were alerted for a 1200 CST flight in anticipation of widespread activity associated with a stationary front across northern Oklahoma. When the B-57 aircraft arrived, the convective system was already well developed, with severe thunderstorms located 40 to 60 n mi northwest of NSSL. The ARSR-1D display at 1330 CST is shown in figure 48. The B-57 is the IFF west-northwest at 32 n mi. The F-100 penetration aircraft making a turbulence measurement run is visible in the storm's interior at 350°. The aircraft to the northeast is an ESSA DC-6 aircraft making temperature and wind measurements in the storm's environment.

At 1330, 2 min into the first approach, the B-57 was 25 n mi south-southeast of the two moderate cells on the extreme south edge of the line. The K_a-band radar was set on 100-mi range. The aircraft heading was 300° at 31,000 ft. The PPI display is shown in figure 49a. Two moderate showers are visible directly ahead of the aircraft. As the approach continued, the operator cycled through an antenna downtilt sequence of -3, -10, -5, -5, -1, and -5°, as shown in figures 49b through 49g.

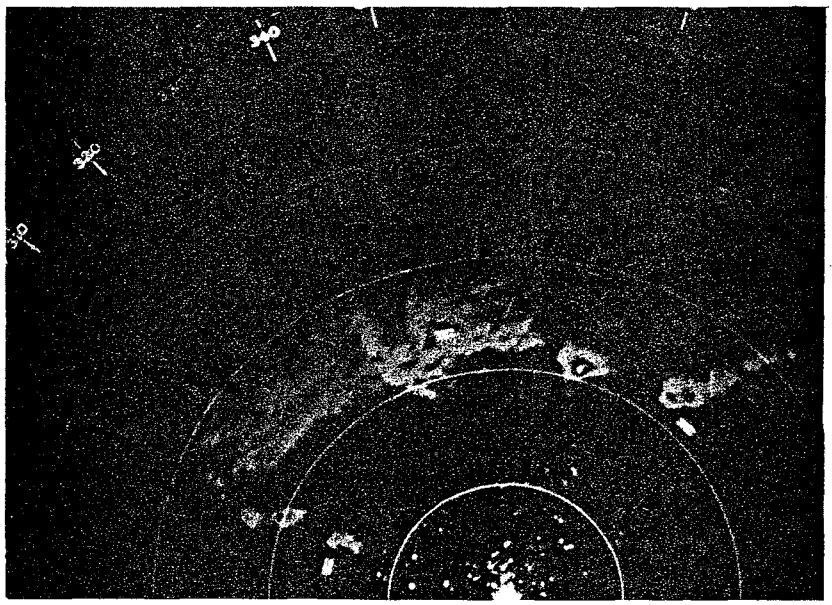

Figure 48. ARSR-1D control radar display, 5 May 1967. Range marks are 25 n mi.

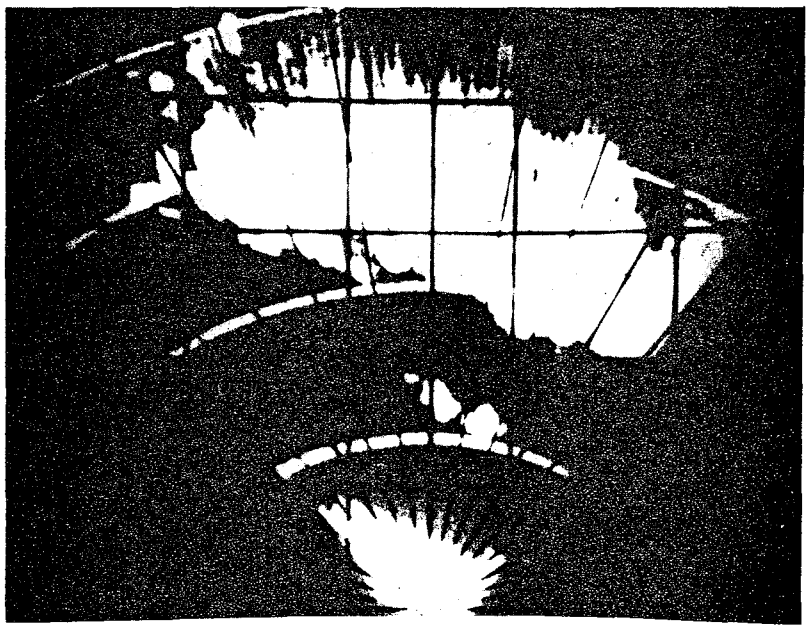

Figure 49a. First approach sequence on the K_a-band radar PPI display. Range marks are 20 n mi.

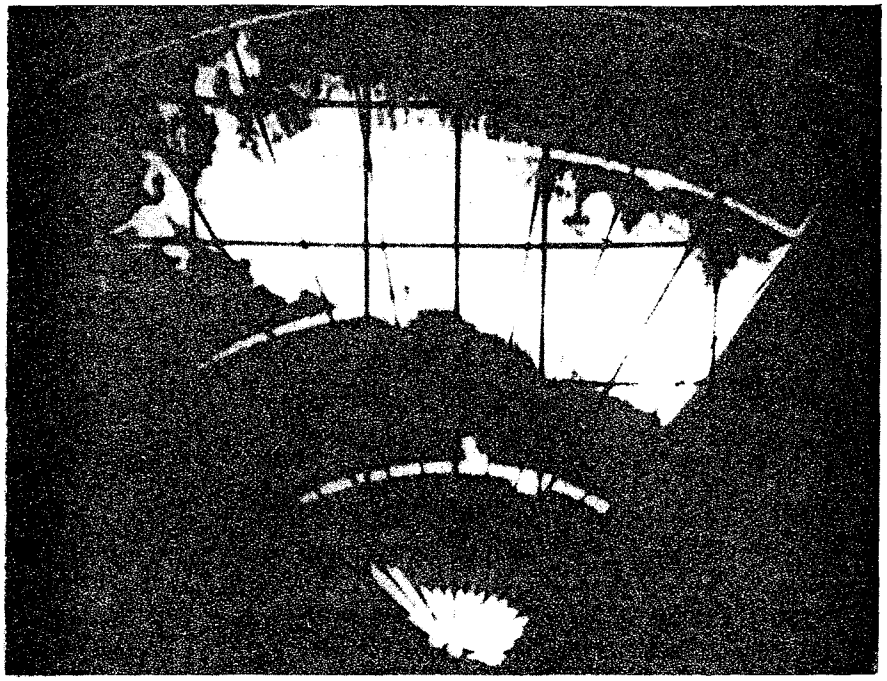

Figure 49b

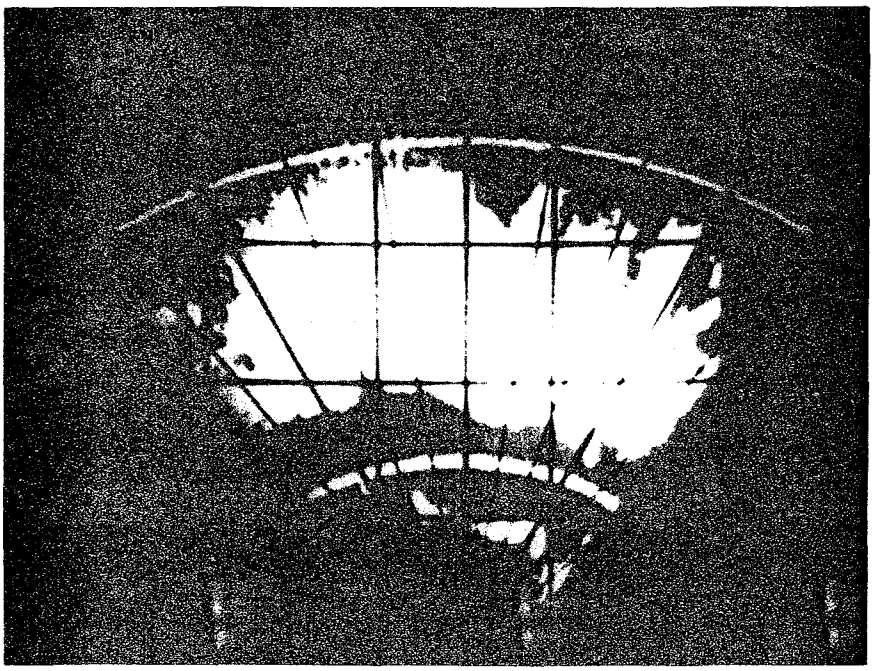

Figure 49c

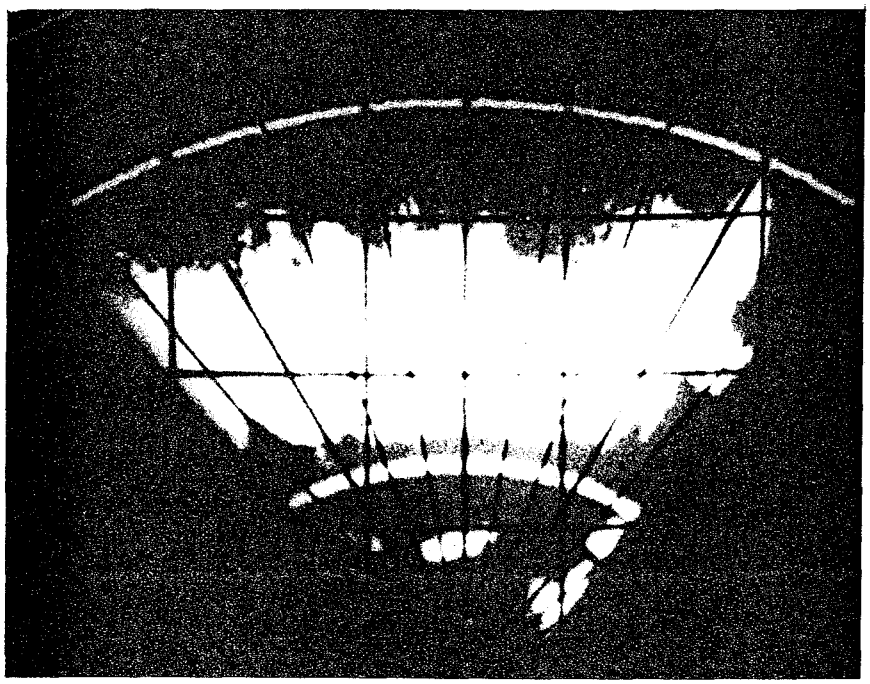

Figure 49d

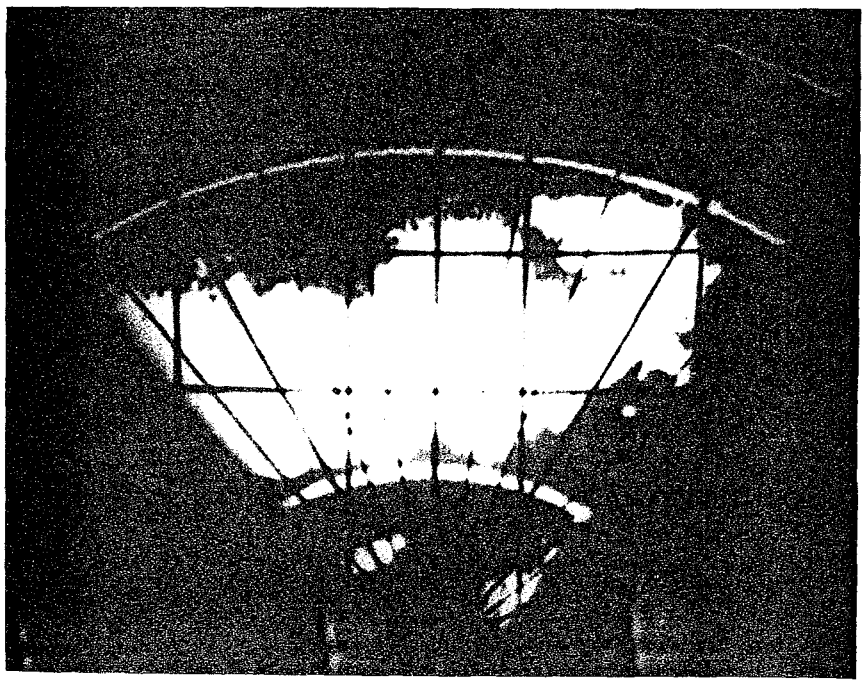

Figure 49e

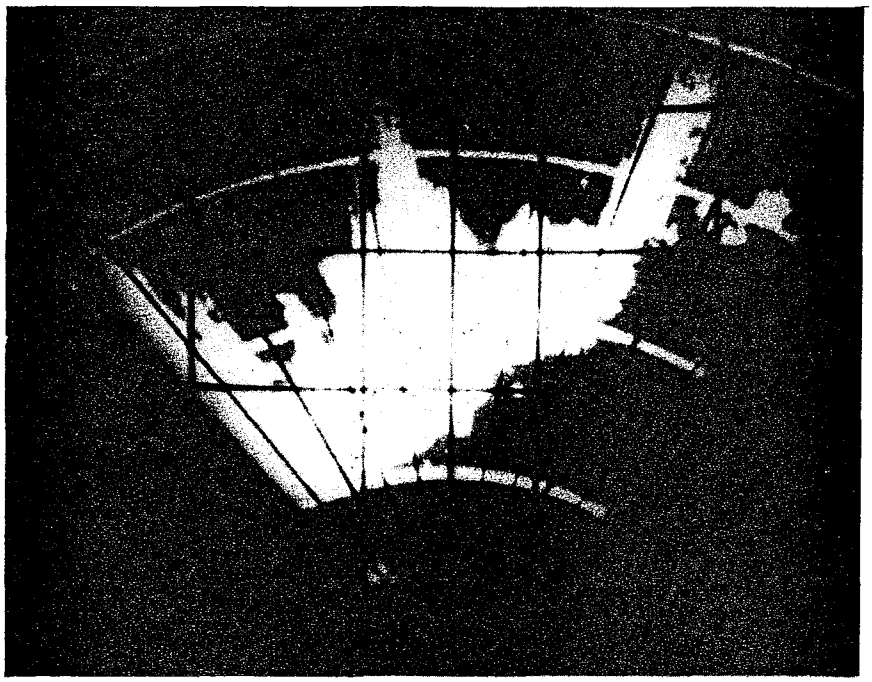

Figure 49f

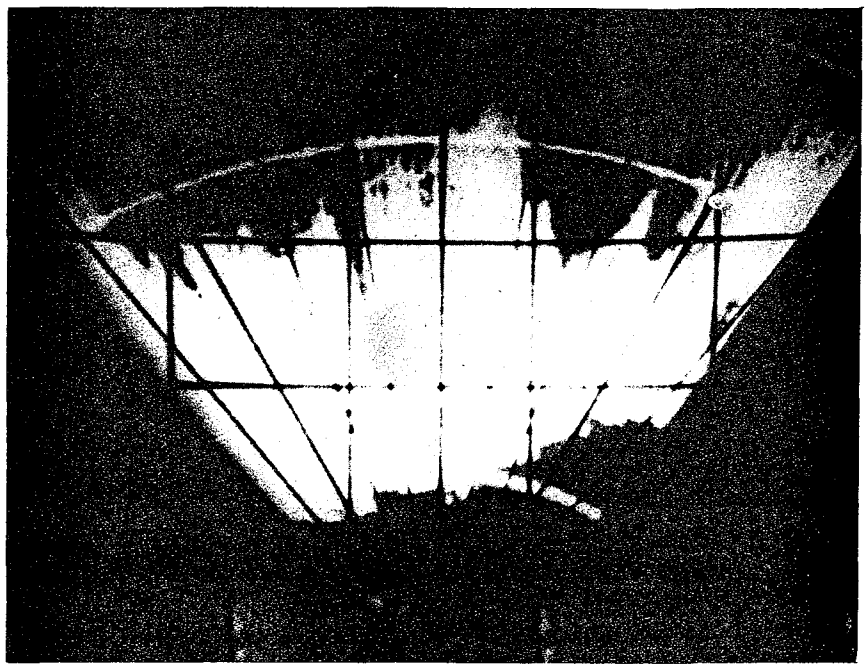

Figure 49g

The rapid range change, occurring simultaneously with the tilt change, makes interpretation very difficult. In the 3-min sequence, the aircraft moved approximately 20 n mi (400 kt), which corresponds to an effective tilt change of 9°. Thus, to sample the storm cross section shown by the -5° display 1 min later requires a further downtilt to -9°.

The patterns in figures 49e and 49f were obtained at beam cross-section altitudes of 24,000 and 22,000 ft, respectively. The aircraft heading was 010° as the first pass ended, and a 180° right turn was made away from the line. The second pass began at 1342 CST. Figure 50 shows the airborne PPI at 1344 CST as the aircraft approached the short line of convection that originated as the two discrete cells noted on the first pass. The corresponding WSR-57 display at 1345 CST is shown in figure 51.

Again, there is noticeable attenuation on the K_a-band display. At this time, the digital system on the WSR-57 radar (Wilk, et al., 1967) numerically recorded the reflectivity distribution. Since the aircraft was west of NSSL, the perspectives of the radars were similar, and the measured reflectivities and observed attenuation could be compared. The technique described in section 3 was used to analyze the WSR-57 data. Figures 52 and 53 show the input B-scan data and the computed output. The calculated attenuation values were used to plot the radial pattern by assuming a back-edge reflectivity of $10 mm^6 m^{-3}$ and decreasing the depth of the far edge of the radial value by an amount corresponding to the calculated attenuation. The general correspondence is good, especially along the 330° radial where the attenuation was most severe.

After completing a short third run, the B-57 returned to the south for a long approach. At 1405 CST, it again turned north and started a final run from 45 n mi at an altitude of 20,000 ft. The display from the ARSR-1D control radar at the FAA Academy is shown in figure 54. All project aircraft used IFF code 05, which is the only one displayed. The northernmost IFF is the F-100 aircraft just completing a penetration. The IFF in the northwest is the P-38 making maximum reflectivity measurements at 12,000 ft. The B-57 is to the southwest, about to turn north for the final pass.

By this time, the leading edge of the southerly moving line of thunderstorms was 40 n mi from NSSL. Most of the activity was weak to moderate, except for a strong cell embedded in the line at an azimuth of 345°. A PPI tilt sequence taken with the WSR-57 radar gave the three-dimensional distribution shown in figures 55a through 55e. Figures 55b and 55c, which are the 2 and 4° cross sections, correspond to 20,000 ft (the aircraft altitude) at the far and leading edges of the echo.

The 1412 CST PPI of the airborne radar, shown in figure 56, corresponds best with the 2° tilt WSR-57 display. Sweep distortion resulted in oblong displays, but when the necessary corrections are made, the echo areas show good agreement. As in the flight of 30 April, the weak precipitation was attenuated to extinction, but reflectivity greater than $10^3 mm^6 m^{-3}$ was displayed.

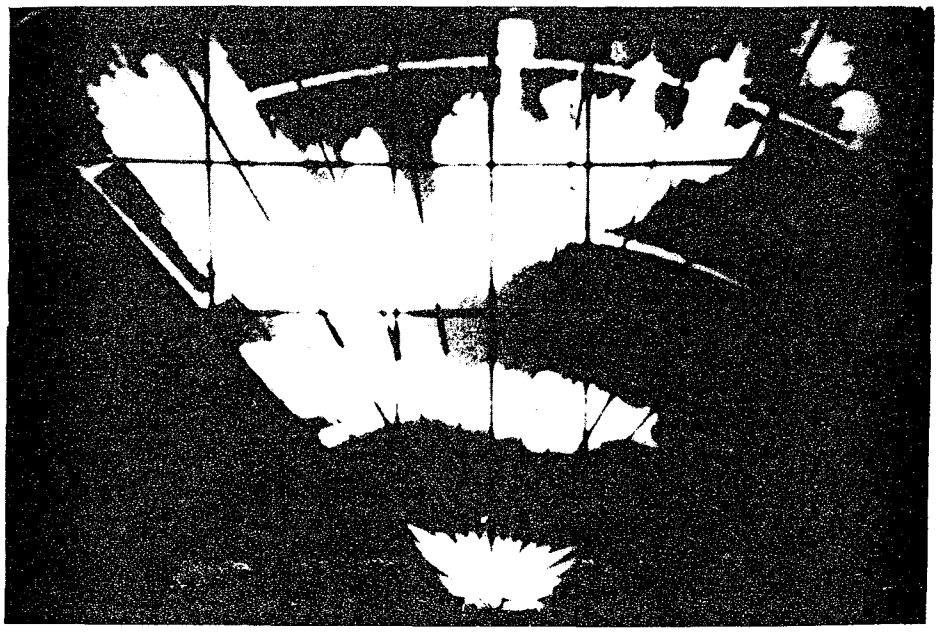

Figure 50. Display during second approach on the K_a-band radar, 1344 CST.

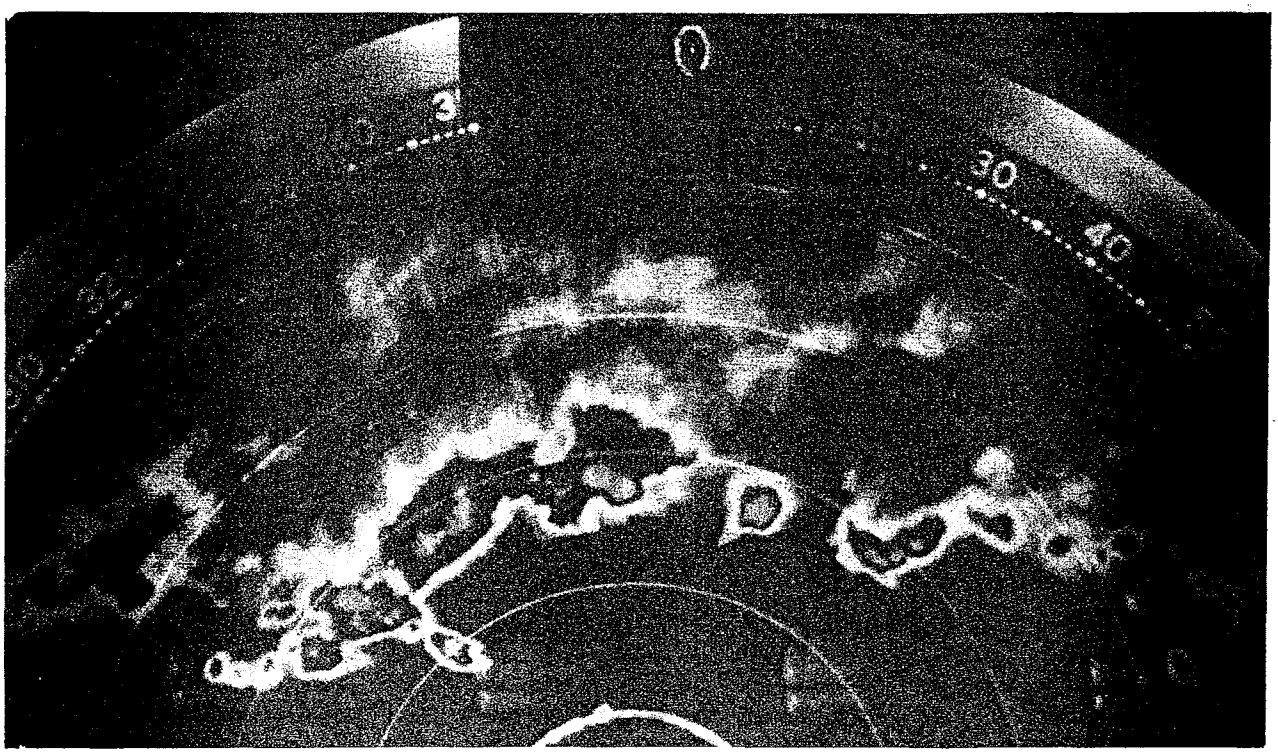

Figure 51. WSR-57 integrated video display. Range marks are 20 n mi, and video core values after cancellation are $\geq 10^4 mm^6 m^{-3}$, 1345 CST.

```
300                         221                 1122223333221          1
302                       233321                 1233333333221
304                     1233331   22            11133332332221
306                    111  1221212       1  1  2233333332211
308                       23332221      11  1112223333322221
310                     23344333222221      1122222222221
312                    1233344423333221            12211
314              222  22333333223222                 21
316           34433 2234323232222221
318          334433 222222222332211    1   1   1  1
320          22322       232233333221111    121
322            2         233333333332211    11  11                    1
324                     1233433333211111111                           1
326                      2334434332211   1
328                     12334433333221                          1
330                     12333443333221 1                        1
332                     122334433332211         1        11
334                      2233444333221              1   11111
336                      22233444333221                 1111
338                        23333333232211               11  111
340                        13343332221 11 11          11121  11
342                        23333322321 1                 1111
344                      122333333332221        1       1  1111
346                    2323333332332221 1    1111     1111
348                    3333443222221 1        1111    1211
350                   12333333322222         11121     11
352                    1223333332333221     1 211  111  1
354                      23344333333211     121    1
356                     123444443333221 1   1211
```

Figure 52. (above) WSR-57 B-scan digital recording for 5 May 1967. Integers are log Z_e. Three-digit column on left is azimuth.

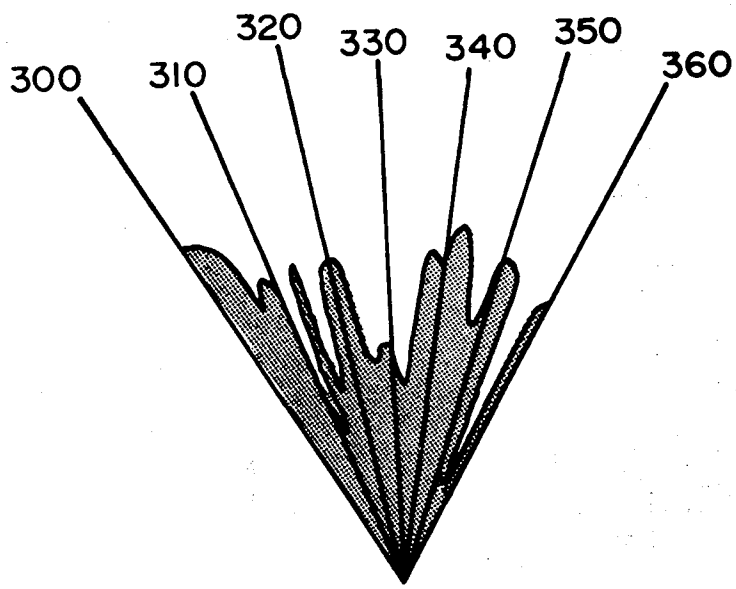

Figure 53. (right) K_a-band PPI display constructed from B-scan with attenuation considered.

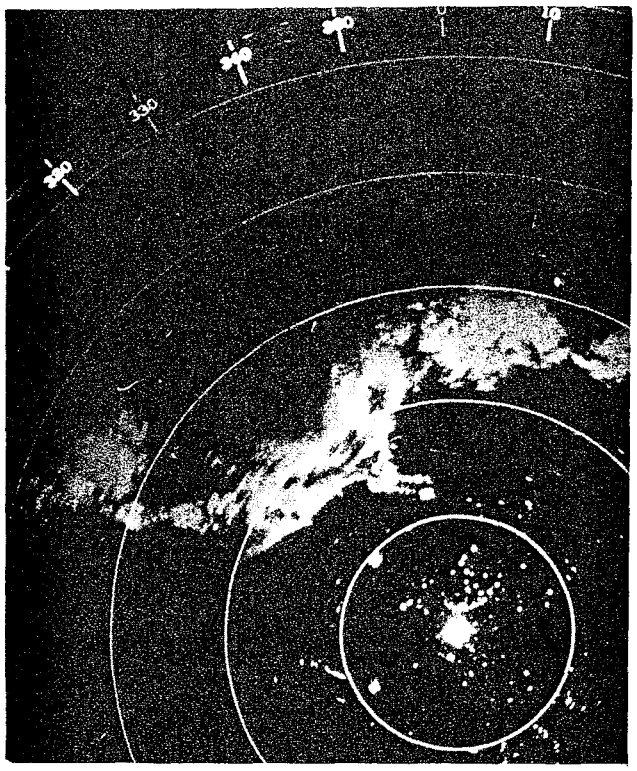

Figure 54. (left) ARSR-1D control radar display at the start of run No. 4, 5 May 1967.

Figure 55a. (below) WSR-57 integrated video at 0° elevation, 1405 CST.

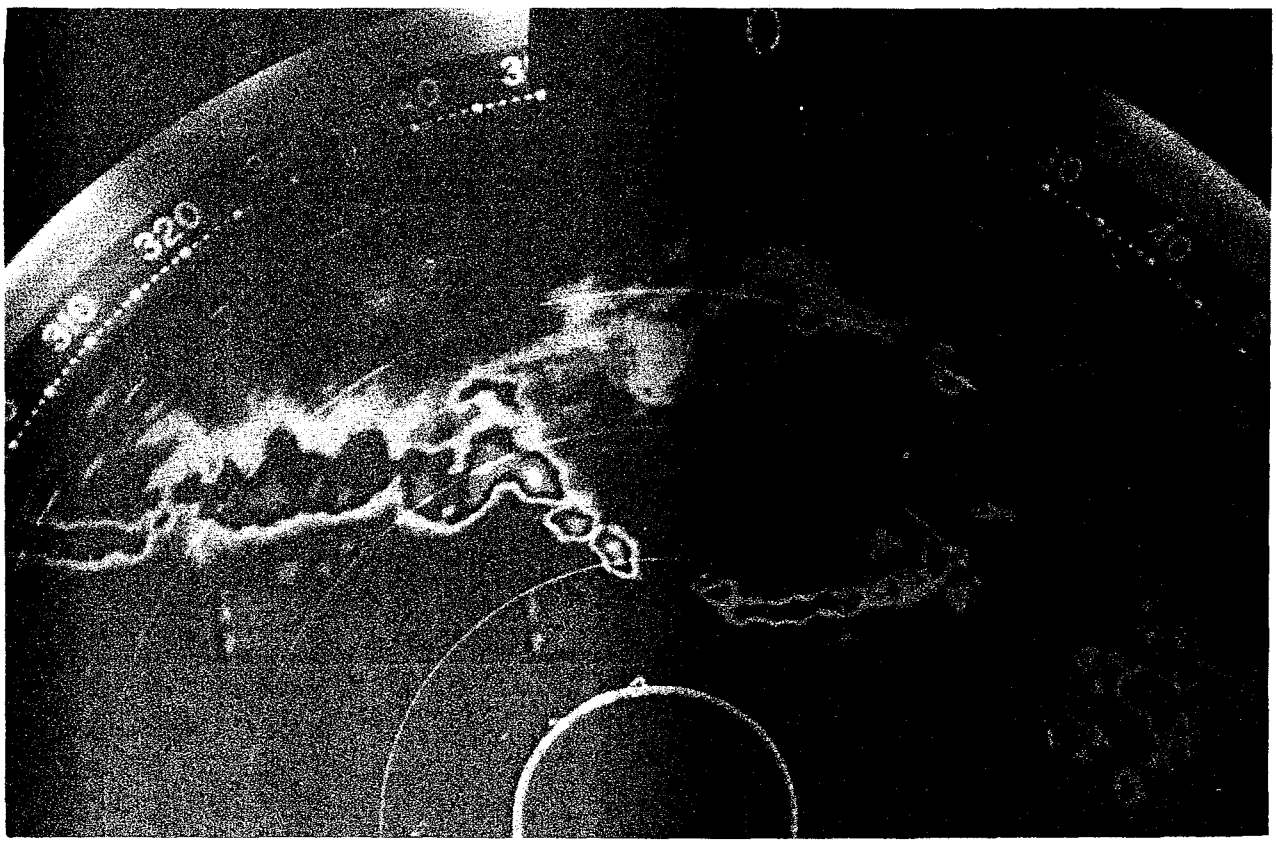

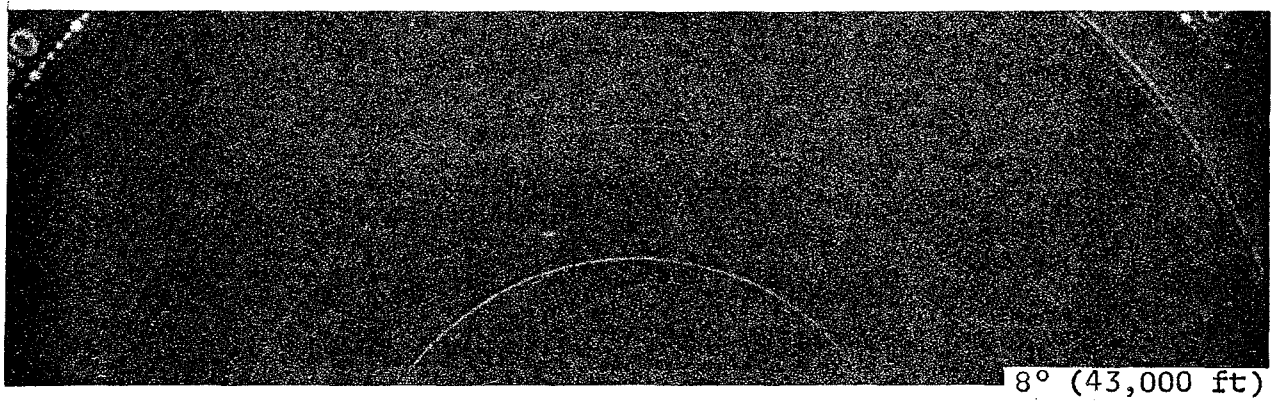

Figure 55e.

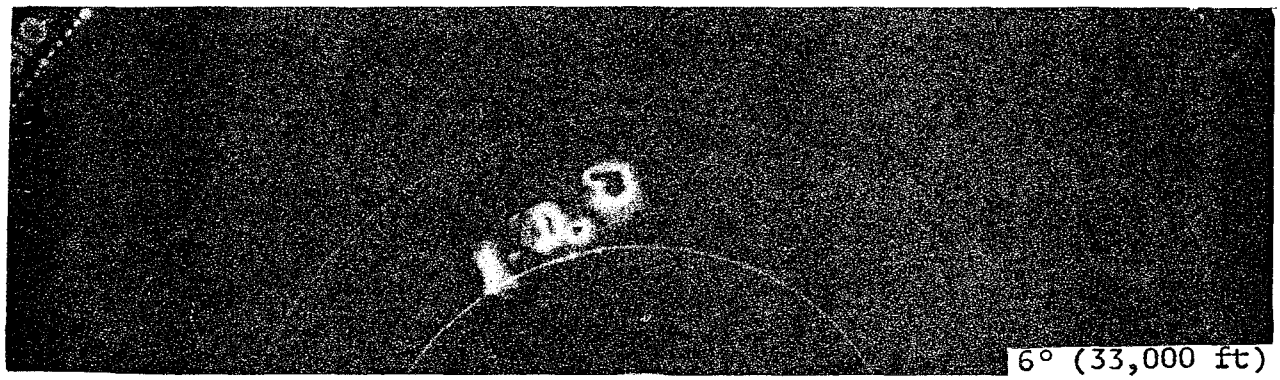

Figure 55d.

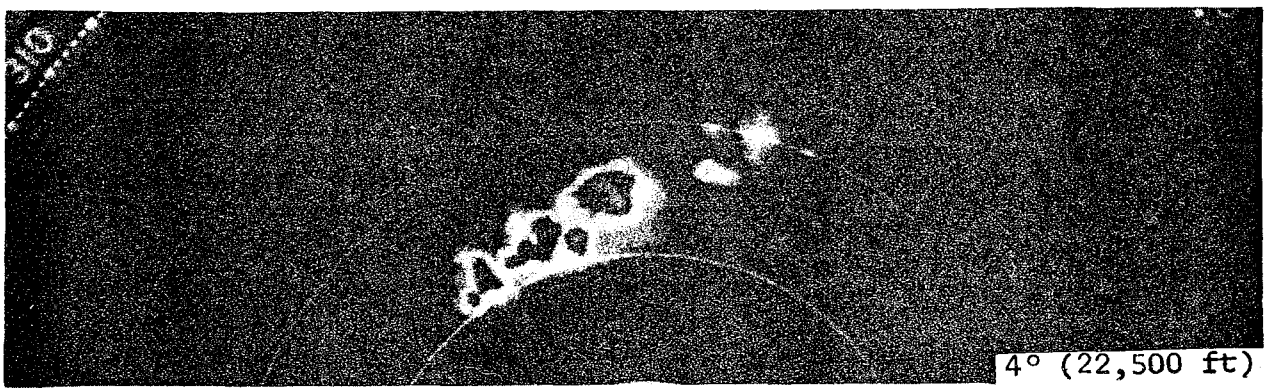

Figure 55c.

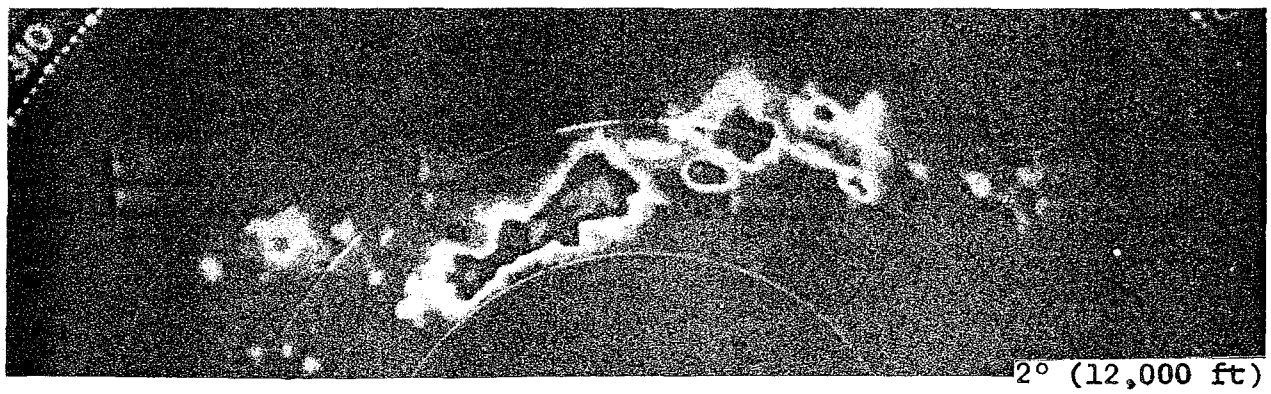

Figure 55b.
WSR-57 radar antenna tilt sequence continuing figure 55a.

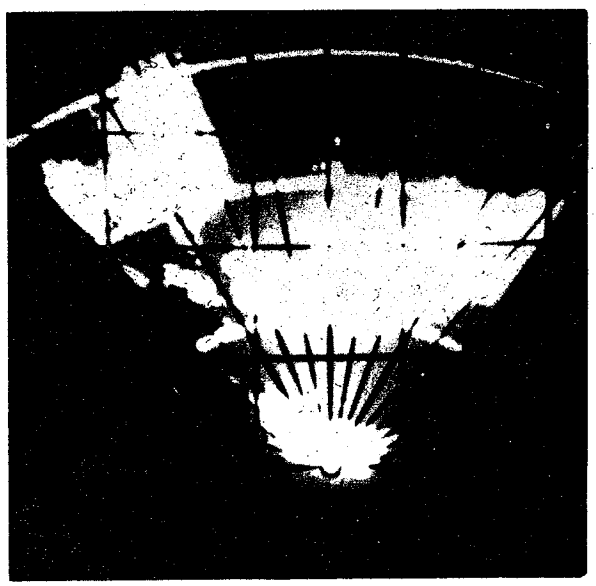

Figure 56. (above) K_a-band PPI display at 1412 CST.

Figure 57. (right) K_a-band RHI display. Aircraft altitude is 20,000 ft. Horizontal overlay lines are at intervals of 5,000 ft.

The operator changed to the RHI mode on a 50-n mi range and obtained what appears to be an excellent vertical profile, shown in figure 57. Close examination, however, shows some interesting discrepancies between this photograph and the WSR-57 measurements. In the 8° tilt photograph, the $Z = 10 mm^6 m^{-3}$ level is barely discernible at 346° at 45 n mi. The corresponding height is approximately 39,500 ft, which is considerably lower than the 50,000-ft top on the K_a-band RHI. Because of the greater sensitivity of the K_a-band radar (an order of magnitude), a discrepancy of 5,000 ft is possible, especially for a decaying thunderstorm. However, the position of the extended turrets at the near edge of the echo and a general structural comparison with the WSR-57 profile suggests that the upper 5,000 ft of the echo may be a result of side lobes. There is obvious attenuation of the low reflectivity area in the far upper portion of the storm. The side-lobe effect is more apparent in this case because of the short range (< 25 n mi) to the storm. A similar effect for ground radars has been noted by Donaldson and Tear (1963). The reader should note that the magnitude of the height extension is related to the magnitude of the lower level reflectivity and, therefore, is still an indication of severity.

In all four approaches to this convective system, the B-57 aircraft was in dense clouds with no visual reference. As on 30 April, the detection was excellent, and reasonable geometric correspondence was found between the displays of airborne and ground radars. The attenuation effect was noticeable and caused widespread loss of the 10 to $10^2 mm^6 m^{-3}$ targets. Losses of signals greater than $10^4 mm^6 m^{-3}$ were confined to convective cores and were rare as the aircraft flew at moderate to high altitudes normal to the squall line. Again, as on 30 April, the sensitivity of the PPI display to antenna tilt was very apparent. The RHI display is extremely helpful in developing a mental picture of the three-dimensional echo distribution.

10. CONCLUSIONS

The X- and C-band airborne radars used in this study are restricted to short-range surveillance because of their relatively small antennas and low sensitivity.

Composited data from airborne and ground radars have clarified several additional problems related to the real-time detection of severe thunderstorms. Among specific findings are:

1. There is sufficient agreement between the displays of convective precipitation by airborne and ground radars to assure that the pilot and controller will reach similar conclusions regarding the location of hazardous weather.

2. Precipitation attenuation does not seriously limit the quantitative capability of X- and C-band airborne radars. It is important to note that this conclusion is based on data collected with airplanes remaining outside of precipitation. Effects of rain and ice on the radome are not considered.

3. Changes of aspect caused by variations in flight altitude, range, and beam stabilization make it extremely difficult to measure representative storm reflectivity.

4. The aspect problem can be greatly alleviated by operating the airborne radar in RHI mode, especially when flying at middle to high altitudes.

5. The K_a-band radar has a significant advantage in resolution and maximum range, but severe precipitation attenuation precludes its use at middle and low altitudes in severe weather situations.

6. The ARSR-1D control radar is excellent for depicting moderate and severe thunderstorms, and the NSSL signal processor enhances its capability. Analysis of PPI photographs can provide statistical information concerning lightning, although additional signal processing equipment would be required to realize a lightning reporting capability in real time.

ACKNOWLEDGEMENTS

Mr. James Cook, with the aid of Collins Radio, instrumented and flew the P-38 aircraft to provide the X- and C-band radar data. Credit for the K_a-band radar observations is due Mr. R. T. Williams, Lawrence Radiation Laboratories and the United States Air Force.

The authors are indebted to Messrs, W. L. Watts, D. Sirmans, and E. Kelly for the design, construction, and operation of the NSSL WSR-57 radar processing system used to obtain the control data for this study. Mr. J. K. Silver prepared the computer programs for the attenuation computations. Dr. E. Kessler, Dr. G. Kinzer, and Mr. L. Merritt provided important guidance concerning theoretical aspects of the study.

Mr. T. J. Simpson and Mr. J. Muncy, Federal Aviation Administration, coordinated the flight program and contributed to the format of the investigation. The control radar data were obtained with the assistance of the FAA Academy, Oklahoma City, Oklahoma.

REFERENCES

Atlas, D. (1958), "Radar lightning echoes and atmospherics in vertical cross section," Proc. Second Conf. Atmospheric Elec., Pergamon Press, New York.

Battan, L. J. (1959), Radar Meteorology (The University of Chicago Press), 161 pp.

Clark, C. and J. T. Dooley (1965), "Radar data acquisition techniques," NSSL Rept. No. 24, 122-130.

Donaldson, R. J., Jr. and R. T. Tear (1963), "Distortions in reflectivity patterns by antenna side lobes," Proc. Tenth Weather Radar Conf., 108-115.

Gunn, K. L. S. and T. W. R. East (1954), "The microwave properties of precipitation particles," Quart. J. Roy. Meteorol. Soc. 80, 522-545.

Hewitt, F. J. (1953), "The study of lightning streamer with 50cm radar," Proc. Phys. Soc. London, B, 66, 895-897.

Hitschfeld, W. and J. Bordan (1954), "Errors inherent in the radar measurement of rainfall at attenuation wavelengths," J. Meteorol. 11, 58-67.

Lhermitte, R. M. and E. Kessler (1965), "A weather radar signal integrator," NSSL Tech. Memo. No. 2, 8 pp; also pp. 301-308 in Proc. Int. Conf. Cloud Physics, Tokyo and Sapporo, Japan, 1965.

Ligda, M. G. H. (1956), "The radar observation of lightning," J. Atmosph. Terr. Phys. 9, 329-346.

Marshall, J. S., C. D. Holtz, and M. Weiss (1965), "Parameters for airborne weather radars," Sci. Rept. MW-48 (ANTC Rept. No. 109), Stormy Weather Group, McGill Univ., Montreal, Canada.

Medhurst, R. G. (1965), "Rainfall attenuation of centimeter waves - comparison of theory and measurement," IEEE Trans. Ant. Prop. 550-564.

Merritt, Lester P. (1967), "Preliminary quantitative analysis of airborne weather radar," ESSA Tech. Memo. ERLTM-NSSL-37.

Miles, V. G. (1952, 1953), "Radar echoes and lightning," Nature 170, 365-366, and "Radar echoes associated with lightning," J. Atmosph. Terr. Phys. 3, 258-262.

Mueller, E. A., A. L. Sims, and R. Cataneo (1967), "Investigation of the quantitative determination of precipitation by radar," Illinois State Water Survey, Interim Rept., Contract No. DA 28-043 AMC-02071(E).

Robertson, S. D. and A. P. King (1946), "The effects of rain upon the propagation of waves in the 1 and 3 centimeter regions," Proc. Inst. Radio Eng. 34, 178-180.

Ryde, J. W. (1946), "The attenuation and radar echoes produced at centimeter wavelengths by various meteorological phenomena," Meteorological Factors in Radio Wave Propagation, 169-188 (Physical Society, London).

Uman, M. A. and R. E. Orville (1964), "Electron density measurement in lightning from stark-broadening of H," J. Geophys. Res. 69, No. 24, 5151-5154.

Wilk, K. E., J. T. Dooley, and E. Kessler (1965), "Weather detection by ARSR-1D, ASR-4 and WSR-57 radars - a comparative study," NSSL Tech. Memo. No. 1.

Wilk, K. E., Walter L. Watts, Dale Sirmans, Roger M. Lhermitte, Edwin Kessler, and Kathryn C. Gray (1967), "Weather radar data system at the National Severe Storms Laboratory," Tech. Circular No. 4, NSSL.

NATIONAL SEVERE STORMS LABORATORY

The NSSL Technical Memoranda, beginning with No. 28, continue the sequence established by the U. S. Weather Bureau National Severe Storms Project, Kansas City, Missouri. Numbers 1-22 were designated NSSP Reports. Numbers 23-27 were NSSL Reports, and 24-27 appeared as subseries of Weather Bureau Technical Notes. These reports are available from the Clearinghouse for Federal Scientific and Technical Information, 5285 Port Royal Road, Springfield, Virginia 22151, for $3.00, and a microfiche version for $0.65. CFTSI numbers are given below in parentheses.

No. 1 National Severe Storms Project Objectives and Basic Design. Staff, NSSP. March 1961. (PB-168207)

No. 2 The Development of Aircraft Investigations of Squall Lines from 1956-1960. B. B. Goddard. (PB-168208)

No. 3 Instability Lines and Their Environments as Shown by Aircraft Soundings and Quasi-Horizontal Traverses. D. T. Williams. February 1962. (PB-168209)

No. 4 On the Mechanics of the Tornado. J. R. Fulks. February 1962. (PB-168210)

No. 5 A Summary of Field Operations and Data Collection by the National Severe Storms Project in Spring 1961. J. T. Lee. March 1962. (PB-165095)

No. 6 Index to the NSSP Surface Network. T. Fujita. April 1962. (PB-168212)

No. 7 The Vertical Structure of Three Dry Lines as Revealed by Aircraft Traverses. E. L. McGuire. April 1962. (PB-168213)

No. 8 Radar Observations of a Tornado Thunderstorm in Vertical Section. Ralph J. Donaldson, Jr. April 1962. (PB-174859)

No. 9 Dynamics of Severe Convective Storms. Chester W. Newton. July 1962. (PB-163319)

No. 10 Some Measured Characteristics of Severe Storms Turbulence. Roy Steiner and Richard H. Rhyne. July 1962. (N62-16401)

No. 11 A Study of the Kinematic Properties of Certain Small-Scale Systems. D. T. Williams. October 1962. (PB-168216)

No. 12 Analysis of the Severe Weather Factor in Automatic Control of Air Route Traffic. W. Boynton Beckwith. December 1962. (PB-168217)

No. 13 500-Kc./Sec. Sferics Studies in Severe Storms. Douglas A. Kohl and John E. Miller. April 1963. (PB-168218)

No. 14 Field Operations of the National Severe Storms Project in Spring 1962. L. D. Sanders. May 1963. (PB-168219)

No. 15 Penetrations of Thunderstorms by an Aircraft Flying at Supersonic Speeds. G. P. Roys. Radar Photographs and Gust Loads in Three Storms of 1961 Rough Rider. Paul W. J. Schumacher. May 1963. (PB-168220)

No. 16 Analysis of Selected Aircraft Data from NSSP Operations, 1962. T. Fujita. May 1963. (PB-168221)

No. 17 Analysis of Methods for Small-Scale Surface Network Data. D. T. Williams. August 1963. (PB-168222)

No. 18 The Thunderstorm Wake of May 4, 1961. D. T. Williams. August 1963. (PB-168223)

No. 19 Measurements by Aircraft of Condensed Water in Great Plains Thunderstorms. George P. Roys and Edwin Kessler. July 1966. (PB-173048)

No. 20 Field Operations of the National Severe Storms Project in Spring 1963. J. T. Lee, L. D. Sanders and D. T. Williams. January 1964. (PB-168224)

No. 21 On the Motion and Predictability of Convective Systems as Related to the Upper Winds in a Case of Small Turning of Wind with Height. James C. Fankhauser. January 1964. (PB-168225)

No. 22 Movement and Development Patterns of Convective Storms and Forecasting the Probability of Storm Passage at a Given Location. Chester W. Newton and James C. Fankhauser. January 1964. (PB-168226)

No. 23 Purposes and Programs of the National Severe Storms Laboratory, Norman, Oklahoma. Edwin Kessler. December 1964. (PB-166675)

No. 24 Papers on Weather Radar, Atmospheric Turbulence, Sferics, and Data Processing. August 1965. (AD-621586)

No. 25 A Comparison of Kinematically Computed Precipitation with Observed Convective Rainfall. James C. Fankhauser. September 1965. (PB-168445).

No 26 Probing Air Motion by Doppler Analysis of Radar Clear Air Returns. Roger M. Lhermitte. May 1966. (PB-170636)

No. 27 Statistical Properties of Radar Echo Patterns and the Radar Echo Process. Larry Armijo. May 1966. The Role of the Kutta-Joukowski Force in Cloud Systems with Circulation. J. L. Goldman. May 1966. (PB-170756)

No. 28 Movement and Predictablity of Radar Echoes. James Warren Wilson. November 1966. (PB-173972)

No. 29 Notes on Thunderstorm Motions, Heights, and Circulations. T. W. Harrold, W. T. Roach, and Kenneth E. Wilk. November 1966. (AD-644899)

No. 30 Turbulence in Clear Air Near Thunderstorms. Anne Burns, Terence W. Harrold, Jack Burnham, and Clifford S. Spavins. December 1966. (PB-173992)

No. 31 Study of a Left-Moving Thunderstorm of 23 April 1964. George R. Hammond. April 1967. (PB-174681)

No. 32 Thunderstorm Circulations and Turbulence from Aircraft and Radar Data. James C. Fankhauser and J. T. Lee. April 1967. (PB-174860)

No. 33 On the Continuity of Water Substance. Edwin Kessler. April 1967. (PB-175840)

No. 34 Note on the Probing Balloon Motion by Doppler Radar. Roger M. Lhermitte. July 1967. (PB-175930)

No. 35 A Theory for the Determination of Wind and Precipitation Velocities with Doppler Radars. Larry Armijo. August 1967. (PB-176376)

No. 36 A Preliminary Evaluation of the F-100 Rough Rider Turbulence Measurement System. U. O. Lappe. October 1967. (PB-177037)

No. 37 Preliminary Quantitative Analysis of Airborne Weather Radar. Lester P. Merritt. December 1967. (PB-177188)

No. 38 On the Source of Thunderstorm Rotation. Stanley L. Barnes. March 1968. (PB-178990)

No. 39 Thunderstorm - Environment Interactions Revealed by Chaff Trajectories in the Mid-Troposphere. James C. Fankhauser. June 1968. (PB-179659)

No. 40 Objective Detection and Correction of Errors in Radiosonde Data. Rex L. Inman. June 1968. (PB-180284)

No. 41 Structure and Movement of the Severe Thunderstorms of 3 April 1964 as Revealed from Radar and Surface Mesonetwork Data Analysis. Jess Charba and Yoshikazu Sasaki. October 1968. (CFSTI No. to be assigned)

No. 42 A Rainfall Rate Sensor. Brian E. Morgan. November 1968. (CFSTI No. to be assigned)

GPO 849-812